nature communications

Article

https://doi.org/10.1038/s41467-025-61534-2

Pancreatic β-cell regeneration in situ by the ALK3 agonist THR-123

Received: 23 November 2024

Accepted: 22 June 2025

Published online: 03 July 2025

Check for updates

Silvia Álvarez-Cubela[1,2], Isabella D. Altilio[1,11], Mayur Doke[1,11], Dagmar Klein[1,11], Alejandro Tamayo[3], Óscar Alcázar[1], Carlos García Santana[1], Mirza Muhammad Fahd Qadir[1], Charles García Alver[4], Francis Cruz[1], Olivia Biggs[1], Jorge David Tovar Castro[1], Belén Navarro-Rubio[5,6], Camillo Ricordi[1,4,7,8], Alejandro Caicedo[3], Peter Buchwald[1,9], Ashutosh Agarwal[4], Elisa Oltra[2], Ricardo Luis Pastori[1,3] ✉ & Juan Domínguez-Bendala[1,7,10] ✉

The demonstration that BMP signaling activates progenitor-like populations within pancreatic ducts supports the potential use of BMP receptor agonists to induce islet neogenesis in situ. In this context, we tested the ability of THR-123, a cyclic peptide with BMP-7-like activity, to regenerate β-cell mass in diabetic mice. We show here that treatment with THR-123 reduces hyperglycemia through the rapid formation of new BrdU-labeled islets, many in apposition to ducts. These islets, unlike those from non-diabetic controls, feature an extensive intrainsular network of ductal tissue. The earlier stages of THR-123-induced β-cell formation were reproduced in live pancreatic slices, an organotypic model that allowed us to visualize ductal cells transitioning to glucose-responsive insulin-expressing cells in real time. scRNAseq analyses further suggest that this transition occurs through a hybrid ducto-acinar stage similar to that previously reported in humans. Taken together, our data support the conclusion that these islets arise predominantly by neogenesis. These results pave the way for the design of pharmacological strategies to treat insulin-dependent diabetes.

Pancreatic progenitor-like cells have been described in the ductal tree of adult humans[1–3] and mice[4]. Specific subpopulations respond to BMP signaling by proliferating, and the withdrawal of the stimulus is permissive for their differentiation along all adult pancreatic lineages (including glucose-responsive β-cells)[1,3]. These cells have been detected in type 1/2 diabetic patients, regardless of disease duration[3]; resolved at the single cell level by scRNAseq of the human ductal tree[3]; and shown to elicit multilineage neogenesis in response to BMP signaling in human/murine pancreatic slices (HPS/mPS)[3,5,6]. A recent serial scRNAseq analysis of HPSs revealed that the activation of ductal progenitors by BMP signaling and their subsequent differentiation into endocrine cells occur through an intermediate ducto-acinar stage[6]. Collectively, these observations are the basis for the hypothesis that pancreatic progenitors may be stimulated in situ through pharmacological means, which could have important therapeutic implications in the context of insulin-dependent diabetes.

[1]Diabetes Research Institute, University of Miami Miller School of Medicine (UM-MSoM), Miami, FL, USA. [2]Escuela de Doctorado, Universidad Católica de Valencia, Valencia, Spain. [3]Department of Medicine, Division of Metabolism, Endocrinology and Diabetes, UM-MSoM, Miami, FL, USA. [4]Department of Biomedical Engineering, UM-MSoM, Miami, FL, USA. [5]Universidad Francisco de Vitoria, Madrid, Spain. [6]CEU Escuela Internacional de Doctorado, Madrid, Spain. [7]Department of Surgery, UM-MSoM, Miami, FL, USA. [8]Department of Microbiology & Immunology, UM-MSoM, Miami, USA. [9]Department of Cellular and Molecular Pharmacology, UM-MSoM, Miami, FL, USA. [10]Department of Cell Biology and Anatomy, UM-MSoM, Miami, FL, USA. [11]These authors contributed equally: Isabella D. Altilio, Mayur Doke, Dagmar Klein. ✉e-mail: rpastori@med.miami.edu; jdominguez2@med.miami.edu

Small cyclic peptide BMP receptor agonists offer an alternative to recombinant BMP proteins[7–9] and have been used systemically in clinical trials with no adverse side effects[10,11]. We report here the formation of new β-cells in diabetic mice as a result of their treatment with one such peptide, THR-123[7,12]. Treated animals exhibited a marked reduction in hyperglycemia vs. controls, and their pancreata showed abundant BrdU$^+$ β-cells, many within or in close proximity to ducts. Additionally, we characterized thick, conspicuous ductal scaffolds within these islets that suggest either active foci of endocrine neogenesis or the remnants thereof. Although our experimental approach is not designed to study whether replication of pre-existing β-cells also plays a role in the formation of new islets[13], the treatment of mPSs with THR-123 within microfluidic chips in vitro exposed the initial stages of β-cell transdifferentiation from ducts in real time, as well as the acquisition of glucose responsiveness by some of these cells as determined by Ca^{2+} imaging. Finally, scRNAseq analysis of mPSs treated for only 5 days with THR-123 revealed the activation of a hybrid ducto-acinar population of cells with progenitor characteristics, a subset of which evolved towards endocrine fates. Comparable transitions were previously reported in human pancreatic slices exposed to BMP-7[6], confirming the conservation of BMP-mediated regenerative mechanisms. Together, our results present a theoretical framework for this modality of β-cell regeneration and open the door to the clinical use of BMP receptor agonists in diabetic patients.

Results

Murine Alk3$^+$ cells are BMP-7-responsive

We have previously established that BMP-7-responsive human progenitor-like cells exist within a ductal subpopulation characterized by the expression of activin-like kinase receptor-3 (ALK3/BMP receptor 1 A) and the purinergic receptor P2Y (P2RY1), a surface marker whose expression correlates with that of nuclear PDX1[1,3]. A more recent independent scRNAseq study of the murine ductal tree[4] suggests the inter-species conservation of these cells. Immunofluorescence (IF) of the pancreas confirmed the existence of ductal Pdx1$^+$/Alk3$^+$ cells in the mouse (Fig. 1a). We hypothesized that cells within this fraction would respond to canonical BMP signaling, as shown by the downstream phosphorylation of SMAD1/5/8 following exposure to BMP-7[14]. To test this hypothesis, we harvested the non-endocrine pancreatic tissue of 10–12-week-old C57BL/6 mice, exposed it to BMP-7 as described in ref. 14, and determined by FACS the relative percentages within the P2RY1$^+$/Alk3$^+$ and P2RY1$^-$/Alk3$^-$ fractions that were pSMAD1/5/8$^+$. As presented in Fig. 1b, c, only the positive fraction showed meaningful BMP-7 responsiveness (maximum stimulation at 15 min measured as % of pSMAD1/5/8$^+$ cells: 2.96 ± 0.25% in the negative vs. 52.33 ± 0.75 % in the positive fraction).

To further characterize the nature of the BMP-7-sensitive cells, we conducted a second set of FACS experiments ($n = 3$) to examine in more depth the makeup of the pSMAD1/5/8$^+$ subpopulations following stimulation of non-endocrine pancreatic tissue with BMP-7. We used CD24 as an additional ductal marker[15] along with Alk3[1,16] (Supplementary Fig. 1a) as well as HNF1β and Sox9, two markers previously described to identify ductal progenitors with organoid-forming capacity[15]. Even before stimulation (0'), the CD24$^+$/pSMAD1/5/8$^+$ fraction was highly enriched in cells expressing Alk3 (75.65 ± 4.80%), HNF1β (80.50 ± 8.64%) and Sox9$^+$ (82.87 ± 6.32%) (Supplementary Fig. 1b, *top*). In contrast, the CD24$^+$/pSMAD1/5/8$^-$ fraction (Supplementary Fig. 1b, *bottom*) exhibited a very low percentage of cells expressing either of these markers. Together, our data show that BMP-7-responsive (pSMAD1/5/8$^+$) ductal subpopulations within murine ducts exhibit characteristics consistent with those previously reported for progenitor-like cells[15]. Importantly, the theoretical possibility that any residual β-cell made it to the analysis cannot be categorically discarded. However, considering that the tissue was depleted of islets beforehand, and that gating in the Alk3$^+$ fraction is expected to selectively exclude Alk3$^-$ β-cells[1,3], this possibility is very remote and would not change in any significant way the conclusions of our analysis.

Treatment with THR-123 reduces hyperglycemia in diabetic mice

We have previously shown that human ALK3$^{bright+}$-sorted cells harbor BMP-7-responsive multipotent progenitors with the capacity to self-arrange into highly organized pancreatic tissue upon transplantation into immunodeficient mice[3]. These outcomes were enhanced when the hosts were treated with the 16-aminoacid cyclic peptide THR-123 (Fig. 1d), an ALK3 agonist with BMP-7-like activity that presents distinct advantages over BMP-7 due to its stability, cost, and ease of synthesis[3,7,14]. The confirmation of the existence of BMP-responsive, progenitor-like cells within murine pancreatic ducts led us to hypothesize that systemic administration of THR-123 would induce the formation of new β-cells in situ through a process involving proliferation and subsequent differentiation of such progenitor cells, as previously described in human pancreatic tissue[1]. To test this hypothesis, we first set out to determine if the agent would reach the pancreas by intraperitoneal (*i.p.*) injection. As shown in Fig. 1e, FAM-tagged THR-123 could be readily detected in the parenchyma/ducts of the pancreas 2 h after administration, which established the feasibility of the approach. Next, we proceeded to make animals diabetic and examine the effect of THR-123 treatment on their glycemic levels over time. A table listing all the strains and regimens tested is shown in Supplementary Fig. 1c. First, 6–8-week-old CD-1 mice were rendered diabetic with the β-cell toxin alloxan (150 mg/kg) (see *Methods*). THR-123 treatment (10 mg/kg) was initiated simultaneously and administered daily *i.p.* for 21 days. Controls received saline with the same frequency (Supplementary Fig. 1d, e). A second set of experiments was conducted with a 20 mg/kg dose (Fig. 1f, g), and a third one using another strain (C57BL/6J) at 10 mg/kg (Supplementary Fig. 1f, g). Animals received BrdU in the water for the entire experiment. Glycemia was monitored for at least 1 extra week, after which mice were euthanized and pancreas, brown fat and peripheral blood harvested. Age-matched non-diabetic mice were also euthanized as positive controls. As shown in Fig. 1f, g and Supplementary Fig. 1d–g, the glycemia of THR-123-treated animals, regardless of the dose, was significantly lower than that of saline-treated mice throughout the experiment ($p < 0.001$ for CD-1–10 mg/kg; $p = 0.0253$ for CD-1–20 mg/kg; and $p = 0.0011$ for C57BL/6J–10 mg/kg). Notably, THR-123 (20 mg/kg) had no effect on the glycemia of non-diabetic animals (Fig. 1h, $p > 0.05$).

BMP signaling has been associated with a reduction of inflammation and increase of insulin sensitivity[17–19], which may also reduce hyperglycemia and explain, at least partially, our observations. To test whether THR-123's effects could be indirectly due to a decrease in inflammatory state, we examined cytokine expression in peripheral blood at the end of the CD-1–10 mg/kg experiment. As presented in Fig. 1i, THR-123 did not reduce expression of the pro-inflammatory cytokines IL-6 ($p > 0.05$), MCP-1 ($p > 0.05$) and TNF1α ($p > 0.05$). Out of the two anti-inflammatory cytokines that we analyzed (IL-10 and IL-17), only the latter was elevated significantly ($p = 0.0338$) by THR-123. Based on these data, a conclusive correlation between THR-123 and the overall inflammatory state could not be established. BMPs have also been linked to white fat browning[20], which could also affect glucose homeostasis in our design. However, neither the average brown fat weight nor the relative expression of uncoupled protein 1 (UCP-1) in overall (white and brown) fat differed significantly between the THR-123 and control groups (Fig. 1i).

Since THR-123 was given to the animals immediately after alloxan administration, another potential explanation of these results is that the agent may be protecting pre-existing islets against chemical destruction, rather than inducing new β-cell formation. This would

https://doi.org/10.1038/s41467-025-61534-2

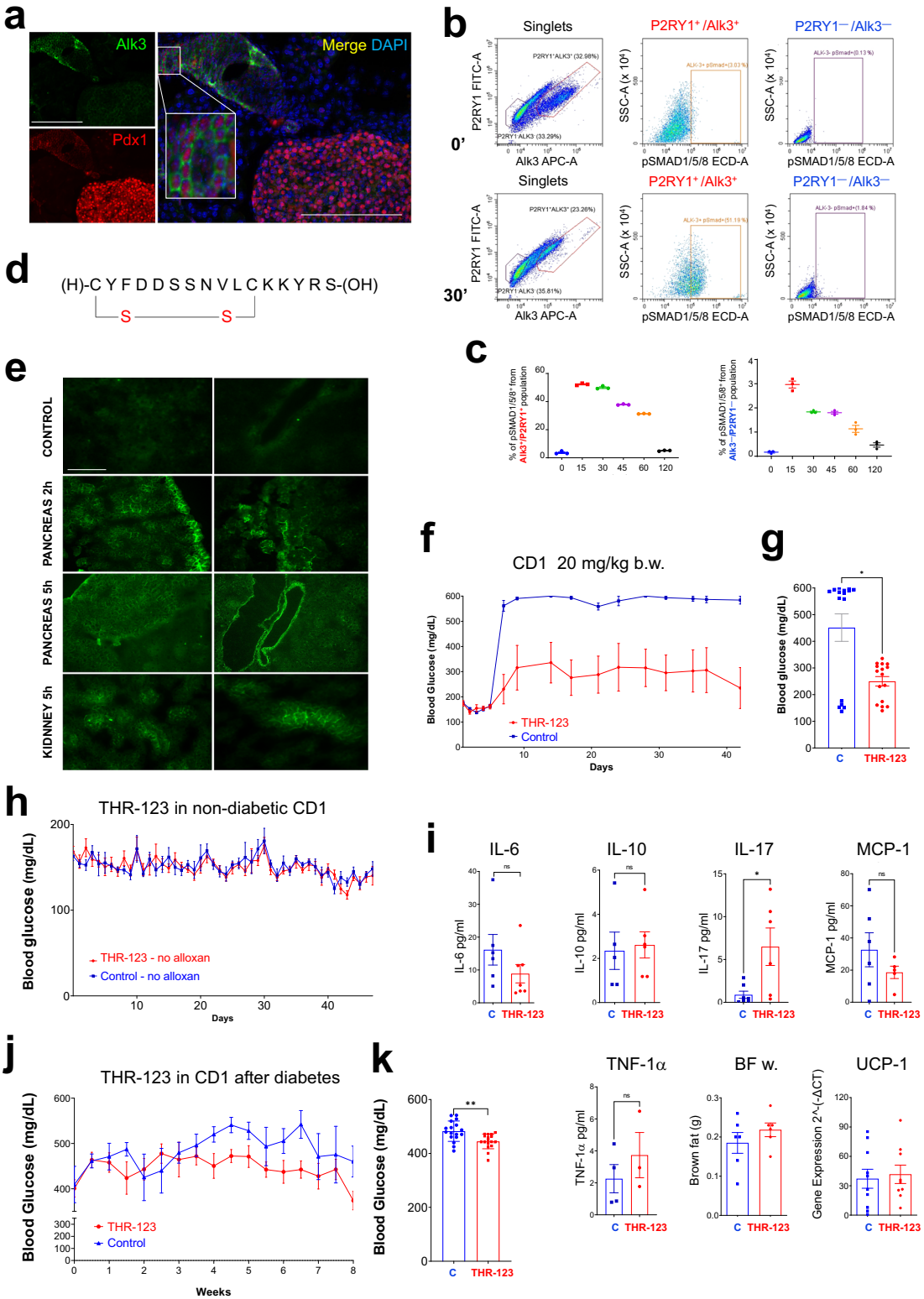

explain why THR-123-treated mice did not become as hyperglycemic as control ones (Fig. 1f). To determine whether this is the case, islets isolated from C57BL/6J mice ($n = 3$ experiments) were either left untreated, exposed to alloxan (2 mM) for 30 min, or treated with alloxan following overnight incubation with THR-123 (10 µM). Aliquots from each group were either subjected to a perifusion assay (to assess glucose responsiveness) or stained with insulin and activated Caspase-3 (to assess viability). As shown in Supplementary Fig. 1h, perifusion did not reveal any meaningful effect of THR-123 at preventing the impairment of glucose-dependent insulin release induced by alloxan (AUC $p = 0.128$), suggesting that its effect is not protective. Pre-treatment with THR-123 did not prevent alloxan-induced islet dis-aggregation even after this short exposure to the toxin (Supplementary Fig. 1i). Due to the accelerated disintegration/death of islets, activated Caspase-3 staining was faint and its quantification incon-clusive (Supplementary Fig. 1j, k). We then performed another in vivo

Fig. 1 | The murine pancreas contains Pdx1$^+$/Alk3$^+$ cells that are responsive to BMP signaling, and systemic treatment of diabetic mice with THR-123 leads to amelioration of hyperglycemia. a Confocal microphotograph (maximal projection) of CD-1 mouse pancreas showing an islet and a duct in apposition (inset, higher magnification of ductal area). The BMP receptor 1A (Alk3, green) only stains the duct, whereas Pdx1 (red) can be seen in the nucleus of both islet β-cells (strong signal) and ductal Alk3$^+$ cells (weaker signal). Size bar: 100 µm. **b** Flow cytometry analysis of mouse non-endocrine cells exposed to BMP-7 in vitro using antibodies against Alk3, P2RY1 (a surrogate surface marker for Pdx1) and pSMAD1/5/8 (the phosphorylated version of SMAD1/5/8). For all the experiments described herein, exocrine tissues were obtained from a total of 30 C57BL/6 mice (10–12-weeks). Upper row: Time point 0 (before treatment). Lower row: 30 min after addition of BMP-7. From left to right: Gating of P2RY1$^+$/Alk3$^+$ and P2RY1$^-$/Alk3$^-$ cells; gating of pSMAD1/5/8$^+$ cells out of the P2RY1$^+$/Alk3$^+$ fraction; and gating of pSMAD1/5/8$^+$ cells out of the P2RY1$^-$/Alk3$^-$ fraction. This analysis reveals that only a very small percentage of cells are pSMAD1/5/8$^+$ prior to the stimulation in either fraction (3.03% and 0.13% in the P2RY1$^+$/Alk3$^+$ and P2RY1$^-$/Alk3$^-$ fractions, respectively). However, after 30 min of BMP-7 exposure, the % of pSMAD1/5/8$^+$ cells is much higher in the positive fraction (51.19 vs 1.84%). **c** The above data are presented in time chart form along with additional time points (15, 30, 45, 60, and 120 min) for both positive (left) and the negative (right) fractions, showing the time-dependent return to unstimulated value ranges by 120 min. $n = 3$ biological replicates/experiment. **d** Structure of the cyclic peptide THR-123. **e** FAM-labeled THR-123 (green) administered by intraperitoneal (*i.p.*) injection can be detected in the pancreatic parenchyma and the kidneys within 2–5 h of administration (top row: non-injected control). Image pairs show two different regions of each analyzed organ. Size bar: 100 µm. $n = 3$ mice for each collection time. **f** Time series chart showing evolution of blood glucose (mg/dL, y axis) over time (days, x axis) of alloxan-treated CD-1 mice injected with 20 mg/kg THR-123 (experimental group, red line) or saline solution (control, blue line) for 3 weeks. **g** Average blood glucose readings ($n = 5$ control and $n = 6$ THR-123-treated biologically independent mice) during the entire experiment for each group, showing a statistically significant decrease in mice treated with THR-123 ($p = 0.0253$). Unpaired two-tailed t-test was performed to compare groups. **h** Time series chart showing evolution of blood glucose (mg/dL, y axis) over time (days, x axis) of non-diabetic CD-1 mice injected with 20 mg/kg THR-123 (experimental group, red line) or saline solution (control, blue line) for 3 weeks ($n = 5$ biologically independent mice/group). **i** Profile of circulating cytokine expression (pg/ml) in peripheral blood of control (blue bars) and THR-123-treated (red bars) mice ($n = 7$ biologically independent mice/group), as well as brown fat weight (grams) ($n = 6$ biologically independent mice/group) and real-time RT-PCR-determined relative expression [$2^{(-\Delta Ct)}$] of uncoupled protein 1 (UCP-1) in total fat for each group [$n = 10$ (control) and $n = 9$ (THR-123) biologically independent mice]. *$p < 0.05$; n.s., no statistically significant difference. Unpaired two-tailed t-test was performed to compare groups. Each data point corresponds to the average of a single mouse. Only data points within the Lower Limit of Quantification (LLOQ)-Upper Limit of Quantification (ULOQ) range are considered valid for analysis. Missing data points fell outside this range. **j** Time series chart showing evolution of blood glucose (mg/dL, y axis) over time (weeks, x axis) of stz-induced diabetic (three consecutive readings over 250 mg/dL) CD-1 mice (**n** = 10 biologically independent animals/group) injected subsequently with 20 mg/kg THR-123 (experimental group, red line) or saline solution (control, blue line) for 3 weeks and followed up for up to 8 weeks. **k** Average blood glucose readings during the entire experiment for each group, showing a statistically significant decrease in mice treated with THR-123 (**$p = 0.0022$). Unpaired two-tailed t-test was performed to compare groups. Error bars throughout this figure (**c**, **f**–**k**) represent the standard error of the means (SEM).

experiment in which mice ($n = 10$/group) were rendered diabetic (i.e., three consecutive readings above 250 mg/dL) prior to THR-123 (20 mg/kg) or saline administration. Additionally, to test the robustness of the model under a different diabetes induction regimen, we used streptozotocin (*stz*) instead of alloxan. As shown in Fig. 1j, k, there is significant ($p = 0.0022$) amelioration of hyperglycemia in the THR-123 group compared to controls, even if the difference was not as marked and the animals did not attain normoglycemia within the studied timeframe. Therefore, whether THR-123 imparts some degree of protection to islets (which we have not been able to confirm experimentally), islet preservation alone cannot explain the latter set of results. Regeneration, in contrast, would be consistent not only with the reduction of hyperglycemia observed in diabetic mice, but also with the glycemic pattern presented in Fig. 1f. Beyond the potential (if unproven) protection of islets in that particular setting, mice that receive THR-123 and alloxan simultaneously would not become overtly diabetic if there was an overlapping destruction (by alloxan) and formation (by THR-123) of pre-existing and neogenic islets, respectively.

In summary, hyperglycemia reduction in THR-123-treated diabetic mice coheres with the hypothesis –supported by our earlier body of work[1,3,5,14]– that BMP receptor agonists induce the expansion of progenitor-like cells that differentiate into functional insulin-producing cells after their withdrawal. While we cannot entirely discard that these experimental outcomes may also be partially due to THR-123's potential metabolic, anti-inflammatory, or islet-protective effects, these alternatives are not fully supported by the available evidence.

Immunofluorescence (IF) analysis of THR-123-treated mice indicates new β-cell formation

To determine if the glycemic improvement of THR-123-treated diabetic mice was due to an enhanced β-cell mass, we performed IF analysis of fixed pancreatic sections from each group (CD-1/THR-123—20 mg/kg and saline controls). We hypothesized that the pancreas of THR-123-treated mice would have a higher number of β-cells than diabetic controls; and that, if newly formed (as opposed to merely preserved), these would also exhibit BrdU incorporation. To test these hypotheses, we stained for insulin (Fig. 2a), insulin/BrdU/DAPI (Fig. 2c), insulin/Alk3/DAPI (Fig. 2d, left) and insulin/BrdU/Alk3/DAPI (Fig. 2d, right) after termination of the experiment. Histological analysis of "tile" composites (whole pancreas) showed normal islets in non-diabetic (Fig. 2a, top) and smaller ones in THR-123-treated diabetic mice (Fig. 2a, middle). At this low magnification, any residual islets in the saline diabetic controls could not be detected (Fig. 2a, bottom). The percentage of β- vs. total (DAPI$^+$) cells was 1.4 ± 0.7% in non-diabetic controls, 0.36 ± 0.06% in THR-123-treated diabetic mice and 0.13 ± 0.04% in saline diabetic controls (Fig. 2b, top). Differences between alloxan/THR-123 and alloxan/saline, as well as those between non-diabetic and THR-123-treated mice, were statistically significant ($p = 0.01$ and 0.02, respectively).

Insulin$^+$ structures in the alloxan/THR-123 sections were often located within the very epithelium of ducts (Fig. 2c–f). It has been suggested that islet-derived β-cells can intercalate into hyperplastic ducts, which could explain the commonly reported observation of β-cells seemingly budding from ducts. However, this hypothesis was formulated in the context of a very specific transgenic model (acinar- or β-cell-traced, 6-month Zn^{2+}-inducible, metallothionein promoter-driven TGFα overexpression), throughout a series of experiments that did not include lineage-tracing of ductal cells, and where any co-localization of insulin and ductal markers was specifically ruled out[21]. In contrast, our analysis of THR-123-treated mice showed abundant insulin$^+$ clusters as if transitioning from Alk3$^+$ cells in ducts, as evidenced by areas of partial co-localization (0.28 ± 0.08%) that were virtually undetected in control diabetic mice (0.024 ± 0.01%, $p = 0.0087$ between the two groups; Fig. 2d–f).

BrdU staining indicates that THR-123 induced significant proliferation of pancreatic tissue (26.8 ± 6.04%) compared to saline-treated controls (5.22 ± 1.58%, $p = 0.02$) and non-diabetic mice, where it was almost negligible (Fig. 2b, bottom). BrdU incorporation was particularly noticeable in Alk3$^+$ ductal and β-cells (Fig. 2c–f, h). The percentage of insulin$^+$ cells that were also BrdU$^+$ in alloxan/THR-123 mice (67.56 ± 12.2%) was significantly higher than that of alloxan/saline animals (15.13 ± 5.44%; $p = 0.012$) (Fig. 2b, middle). A similar trend was also observed with Alk3$^+$/BrdU$^+$ vs. total Alk3$^+$ (43.78 ± 7.95% in alloxan/

https://doi.org/10.1038/s41467-025-61534-2

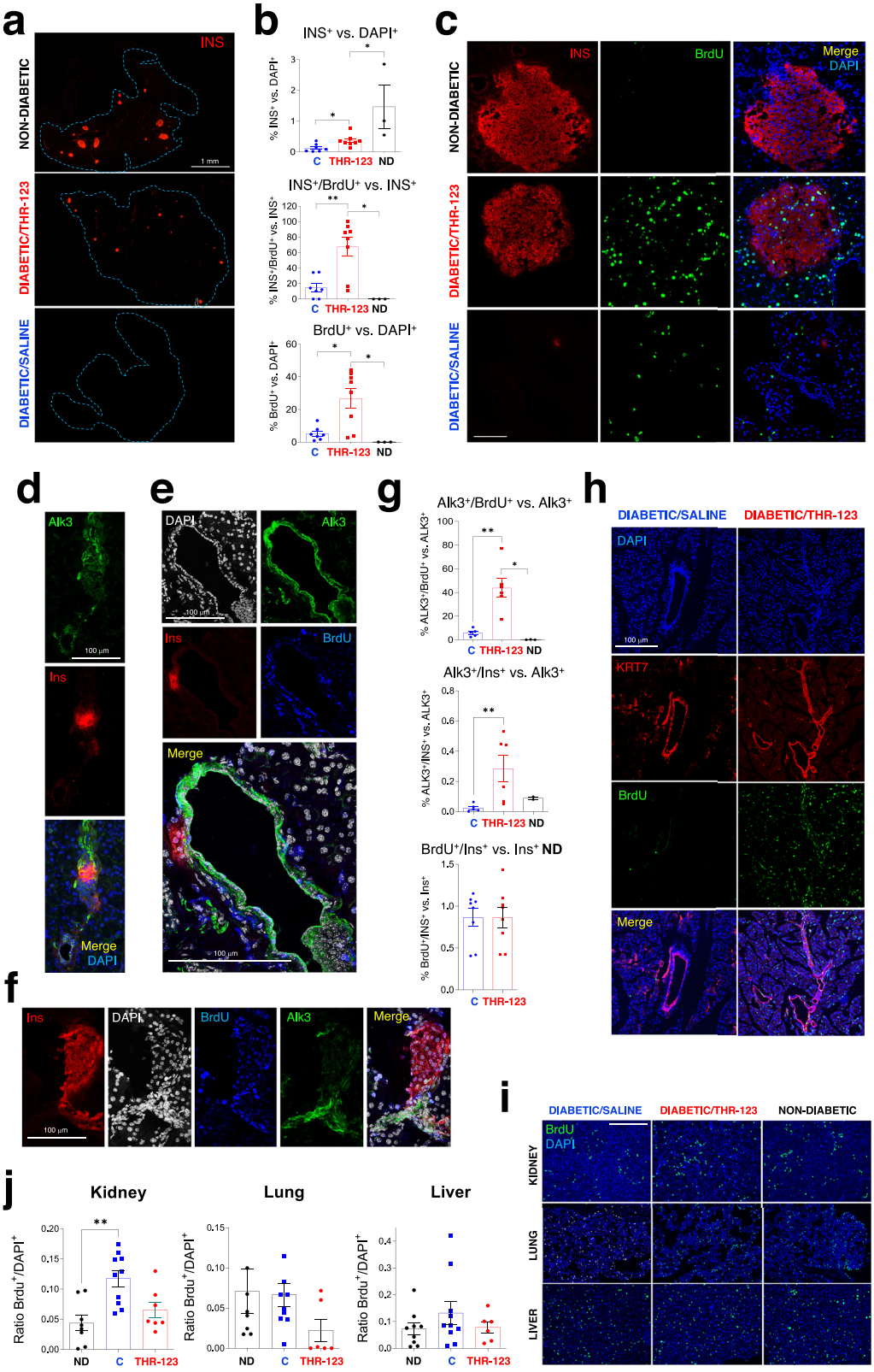

THR-123 compared to 6.00 ± 1.46% in alloxan/saline, p = 0.0043) (Fig. 2g, top). Importantly, THR-123 did not induce proliferation above baseline in the β-cells of non-diabetic mice (Fig. 2g, bottom; p = 0.099) or in organs other than the pancreas in diabetic ones (Fig. 2I, j). Collectively, these observations suggest that only a diabetic/stressed tissue microenvironment (e.g., the pancreas after alloxan treatment) may be permissive for THR-123-mediated regeneration to occur. Consistent with this hypothesis, pancreatic Alk3 expression was found to be elevated in diabetic mice vs. healthy controls (Supplementary Fig. 2a).

Long-term follow-up reveals post-treatment growth of neogenic islets and extensive intrainsular ductal structures

While most animals were euthanized 1 week after termination of the 3-week treatment, a few were followed up for 3 months. IF revealed

Fig. 2 | THR-123-treated mice exhibit signs of new endocrine cell formation. **a** Tiled composite images of representative cross-sections of the entire pancreas of non-diabetic (top), diabetic/THR-123-treated (middle), and diabetic/saline-treated (bottom) CD1 mice. The contour of the organ is marked by blue dotted lines. Samples were stained for insulin (red). Residual β-cells in the alloxan/saline group are not discernable at this low, panoramic magnification. Size bar: 1 mm. **b** Bar graphs showing the area % of insulin-expressing cells out of that of total DAPI$^+$ signal (top); % of insulin$^+$ cells that also express BrdU out of total insulin-expressing cells (middle); and overall % of BrdU-expressing cells out of total DAPI$^+$ (bottom). Saline (C), THR-123, and nondiabetic (ND) columns in blue, red, and black, respectively. $n = 3$ non-diabetic, $n = 4$ diabetic/THR-123-treated, and $n = 4$ diabetic/saline-treated biologically independent CD1 mice were used. Unpaired two-tailed t-tests were performed to compare groups. Error bars: standard error of the means. *p < 0.05; **p < 0.01. Ins$^+$ vs DAPI$^+$: Ctrl vs THR-123, $p^=0.014$; ND vs THR-123, $p = 0.024$. Ins$^+$/BrdU$^+$ vs. Ins$^+$: Ctrl vs THR-123, p = 0.0092; ND vs THR-123, $p = 0.0121$. BrdU$^+$ vs. DAPI$^+$: Ctrl vs THR-123, $p^=0.0289$; ND vs THR-123, $p = 0.012$. Each data point is the average obtained from the analysis of a single mouse. **c** Example of islet regions (insulin, red; BrdU, green; and DAPI, blue) from non-diabetic (top), diabetic/THR-123-treated (middle) and diabetic/saline-treated (bottom) mice. Size bar: 50 µm. **d** Confocal Alk3 (green) and insulin (red) co-staining reveals clusters of insulin$^+$ cells within ductal structures. Size bar: 100 µm **e** Abundant BrdU signal (blue) is typically detected in those ducts harboring insulin$^+$ cells (panels, showing individual channels and merge). Size bar: 100 µm. **f** Example of an islet (Ins$^+$, red) in apposition to a duct (Alk3$^+$, green) where virtually all Ins$^+$ cells (and most Alk3$^+$) are BrdU$^+$, reflecting new formation during the treatment. An area of Alk3$^+$ and Ins$^+$ colocalization is also detected at the bottom right corner of the structure. DAPI, white. Merge, all channels. Size bar: 100 µm. **g** Bar graphs showing the area % of Alk3$^+$ cells that also express BrdU relative to the total number of Alk3$^+$ cells (top); cells that co-express Alk3 and insulin relative to the overall number of Alk3$^+$ cells (middle); and cells that co-express BrdU and insulin relative to the total number of insulin$^+$ cells in non-diabetic (ND) mice (bottom). Saline (C), THR-123, and non-diabetic (ND) columns in blue, red, and black, respectively. Unpaired two-tailed t-tests were performed to compare groups. Alk3$^+$/BrdU$^+$ vs Alk3$^+$: Ctrl vs THR-123, $p = 0.0043$; ND vs THR-123, $p = 0.0238$. Alk3$^+$/Ins$^+$ vs Alk3$^+$: Ctrl vs THR-123, $p^=0.0087$. Error bars: standard error of the means. *p < 0.05; **p < 0.01. Each data point is the average obtained from the analysis of a single mouse. **h** Extensive ductal cell proliferation (BrdU, green; KRT7, red) is detected in diabetic mice injected with THR-123 (right column), but not in saline-treated ones (left column). DAPI: nuclear counterstain (blue). Size bar: 100 µm. **i** Representative microphotographs of kidney (top row), lung (middle), and liver (bottom) tissue showing BrdU incorporation (green) against DAPI (blue) in saline-treated diabetic (left column), THR-123-treated diabetic (middle column), and non-diabetic (right column) mice. The latter were given BrdU in the drinking water during the same length of time the other two groups were treated. **j** Bar graphs showing the ratio BrdU$^+$/DAPI$^+$ (y axis) in kidney (left), lung (middle) and liver (right). Saline (C), THR-123, and nondiabetic (ND) columns in blue, red, and black, respectively. Unpaired two-tailed t-tests were performed to compare groups. Error bars: standard error of the means. With the exception of kidney, where control diabetic mice displayed a higher rate of BrdU incorporation than non-diabetic ones ($p = 0.013$), no statistically significant differences could be appreciated between groups.

that their islets were generally larger than at 1 month (Fig. 3a, left), suggesting that THR-123 initiated a process that continued after the treatment stopped. Intriguingly, these islets often featured a more widespread internal scaffold of Krt7$^+$ ductal tissue (Fig. 3a, left) than that in age-matched non-diabetic mice (Fig. 3a, right). Notably, these networks could be detected with antibodies against Krt7 but were negative for other ductal markers such as Alk3 or Krt19. Our findings are consistent with earlier reports showing intrainsular duct staining with Krt7, but not Krt19 or Krt20[22,23].

The observation that networks of this extent were not present in control mice prompted us to repeat the experiment accounting for a longer follow-up to confirm the latter observation and to test the hypothesis that the growth of islets would plateau after reaching a normal size. We also extended the THR-123 treatment course from 3 to 4 weeks. Thus, 40 CD-1 mice were rendered diabetic (3 consecutive readings >250 mg/dL of blood glucose) and then treated daily with either 20 mg/kg of THR-123 ($n = 20$) or saline ($n = 20$) for 4 weeks. Half of the animals in each group were euthanized and their pancreata analyzed at weeks 10 and 20 (6 and 16 weeks after treatment termination, respectively). A third group of 10 age-matched non-diabetic mice was monitored in parallel. BrdU was given as before but, given potential toxicity, only for a maximum of 6 weeks for each group (weeks 4–10 in 10-week group, and for 7 days every third week in the 20-week group; see research design chart in Supplementary Fig. 2b). Glycemia was assessed periodically throughout, and IPGTTs and basal insulin/C-peptide determined in selected animals at 10 and 20 weeks prior to euthanasia and whole-pancreas sagittal plane scanning IF analysis. As shown in Supplementary Fig. 2c, THR-123 decreased hyperglycemia vs. controls (maximum glycemic separation of ~200 mg/dL at 16 weeks) and led to normoglycemia by week 20. Interestingly, we also noticed that control mice had a delayed decrease of hyperglycemia (although still in the diabetic range) between weeks 16 and 20. Spontaneous return to normoglycemia has been reported[24,25] and may reflect natural (if slower) regenerative processes. While still impaired, treated mice had more efficient glucose clearance than untreated controls and exhibited higher fasting insulin/C-peptide secretion at both 10 and 20 weeks. These values were higher for both groups at the latter point (Supplementary Fig. 2d). Further confirming that the amelioration of hyperglycemia induced by THR-123 was due to β-cell regeneration rather than a potential improvement of insulin sensitivity, there were no statistically significant differences between each group's Matsuda index at either time point (Supplementary Fig. 2d).

Islets of near normal size (Fig. 3b, c, Supplementary Fig. 2e) could be readily detected in the experimental group at both 10 and 20 weeks, usually near ducts (Fig. 3b, right; Supplementary Fig. 2e, right). However, islets from untreated mice (Fig. 3c) appeared largely devoid of β-cells (Supplementary Fig. 2e, left) or consisted at most of small clusters thereof (Fig. 3b, left). The relative percentage of insulin-expressing cells was significantly higher in the THR-123 group at both time points (Fig. 3d), as was the case with the intrainsular Krt-7 area (Fig. 3e) and its mean fluorescence intensity (Fig. 3f). Of note, there was little BrdU incorporation to β-cells in either group at 10 weeks (Fig. 3g, left). Unlike in the first set of experiments, where BrdU was given throughout, mice of the 10-week group received it only from week 4 onwards (Supplementary Fig. 2b). This suggests that most of the new β-cells formed during THR-123 treatment, and that the subsequent growth of islets may ensue by differentiation and coalescence. In contrast, since animals in the 20-week group received BrdU periodically throughout the treatment (Supplementary Fig. 2b), their islets had very high BrdU labeling (Fig. 3g, right). This was true not only of those of the THR-123 group, but also of the much fewer β-cells detected in saline controls: even though many islets in the pancreas of control mice were very small and devoid of BrdU (Supplementary Fig. 2g), many also had significant BrdU labeling (~14% of the total β-cell number, Fig. 3g, right). This observation implies, as noted, that the injured pancreas is also regenerating its β-cell compartment, albeit at a slower pace. Of note, the pancreas of THR-123-treated mice exhibited simultaneously large, BrdU-replete islets, and small, BrdU-negative ones (Supplementary Fig. 2f). While we cannot discard that the latter may represent the upper or lower sections of larger islets that may in fact be labeled with BrdU in other planes, the similitude with the pattern observed in age-matched, saline-treated diabetic mice (Supplementary Fig. 2g) suggests that these are probably pre-existing islets that resisted the alloxan treatment from the beginning. If so, the data of Supplementary Fig. 2f would indicate that THR-123 induces the formation of new islets without significantly affecting residual ones. Finally, the quantification of the percentages of BrdU-labeled cells within each of the examined cell types (Ins$^+$, Krt7$^+$, and Ins$^-$/Krt7$^-$), indicates that THR-123 treatment results in the preferential incorporation of BrdU within the endocrine

https://doi.org/10.1038/s41467-025-61534-2

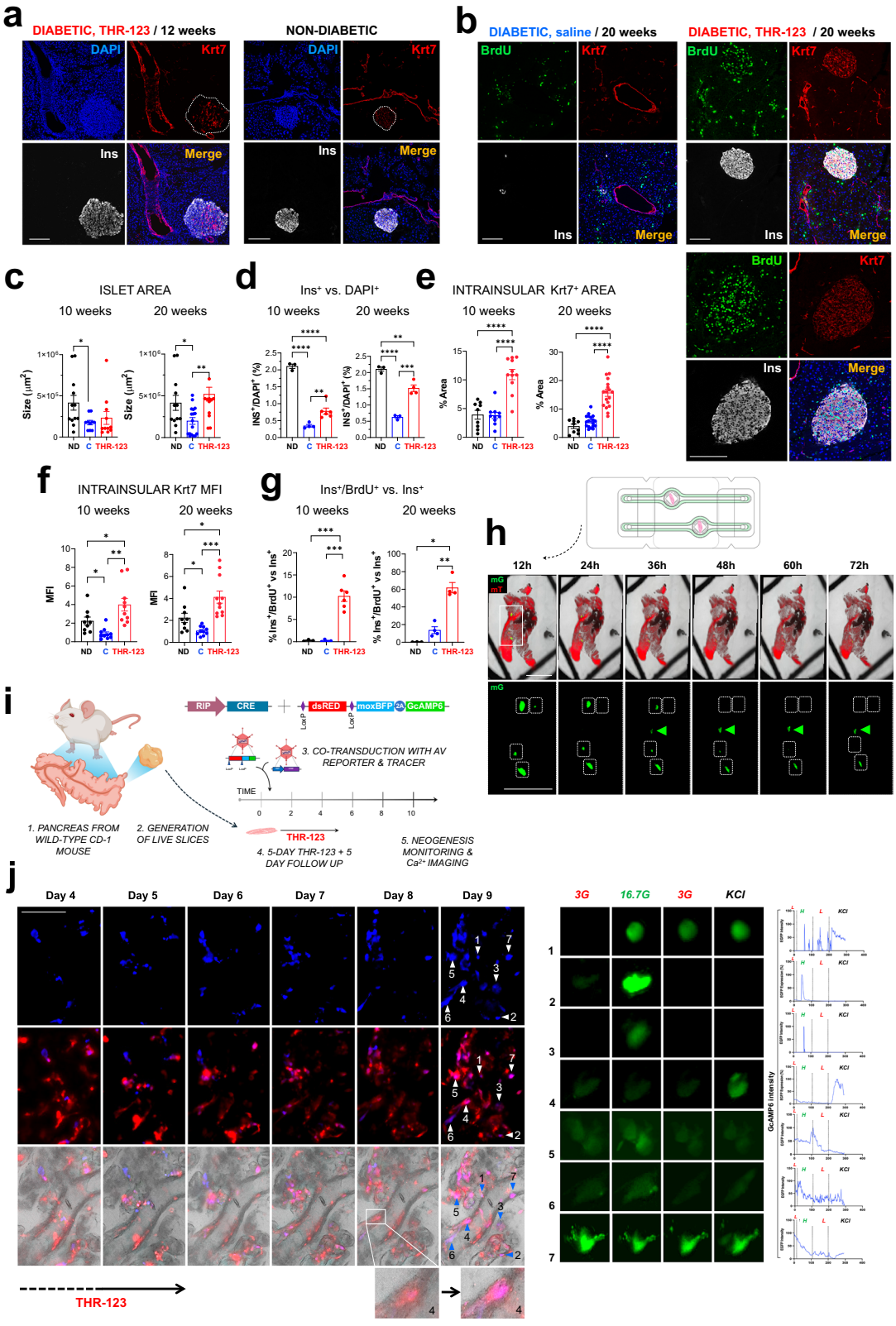

and ductal compartments, with a much lower proportional rate in other tissues (Supplementary Fig. 3a).

Real-time monitoring of ductal-mediated neogenesis

While the previous data indicate that islets regenerate in response to THR-123 treatment, we could only make inferences about the nature of process after euthanizing the animals. We hypothesized that the pancreatic slice platform[5] would enable the real-time visualization of the earlier stages of endocrine regeneration induced by the agent. To test this hypothesis, we exposed mPSs from alloxan-treated *Ins2*^{CRE}/*mTmG* mice [where non-β-cells express membrane-bound tdTomato (red), and insulin expression elicits a Cre-mediated recombination that renders β-cells EGFP-positive[5]] to THR-123 for 5 days and then placed them within a bespoke microfluidic chip[26] for an additional 72 h. The

Fig. 3 | High intrainsular Krt7 content suggests the involvement of ductal cells in THR-123-mediated endocrine regeneration, and the earlier stages thereof can be monitored in real time using pancreatic slices. a Confocal microphotographs of regions containing a single islet next to a large duct from a THR-123-treated diabetic mouse at 3 months (left 4 panels) or from a non-diabetic one (right four panels), showing comparatively more widespread intrainsular ductal tissue (Krt7, cytokeratin 7, red; Ins, insulin, white; DAPI, nuclear staining, blue; merge: all three channels). Size bar: 75 µm. **b** Confocal microphotographs of the pancreas of diabetic mice after long-term (20 weeks) follow up (saline-untreated, left four panels; THR-123-treated, right 8 panels: low and high magnification in top 4 and bottom 4, respectively). Krt7, cytokeratin 7, red; Ins, insulin, white; BrdU, green; merge, all three channels plus DAPI (blue). Size bars: 75 µm. **c** Bar graphs showing average islet area (µm²) at 10 and 20 weeks. 10 weeks: ND vs Ctrl, $p = 0.0234$; 20 weeks: ND vs Ctrl, $p = 0.0434$; Ctrl vs THR-123, $p = 0.0025$. **d** Bar graphs showing percentage of insulin⁺ area relative to total DAPI⁺ area at 10 and 20 weeks. 10 weeks: ND vs Ctrl, $p < 0.0001$; Ctrl vs THR-123, $p = 0.0041$; ND vs THR-123, $p < 0.0001$. 20 weeks: ND vs Ctrl, $p < 0.0001$; Ctrl vs THR-123, $p = 0.0008$; ND vs THR-123, $p = 0.0063$. **e** Bar graphs showing percentage of intra-islet Krt7⁺ area relative to total islet area at 10 and 20 weeks. 10 weeks: Ctrl vs THR-123, $p < 0.0001$; ND vs THR-123, $p < 0.0001$. 20 weeks: Ctrl vs THR-123, $p < 0.0001$; ND vs THR-123, $p < 0.0001$. **f** Bar graphs showing the mean fluorescence intensity (MFI, arbitrary units) of intrainsular Krt7⁺ signal at 10 (left) and 20 (right) weeks. 10-weeks: ND vs Ctrl, $p = 0.0139$; ND vs THR-123, $p = 0.0453$; Ctrl vs THR-123, $p = 0.0012$. 20 weeks: ND vs Ctrl, $p = 0.0255$; ND vs THR-123 $p = 0.0146$; THR-123 vs Ctrl, $p = 0.0002$. **g** Bar graphs showing the percentage of insulin⁺ area that co-localize with BrdU⁺ relative to the total insulin⁺ area at 10 (left) and 20 (right) weeks. 10 weeks: ND vs. THR-123: $p = 0.0004$; Ctrl vs. THR-123: $p = 0.0003$. 20 weeks: ND vs. THR-123, $p = 0.013$; Ctrl vs. THR-123, $p = 0.008$. For all analyses in panels (c–g), serial paraffin sections ($n = 3$ sections per mouse) were used. Sample sizes were as follows: THR-123 group, 10 weeks: $n = 6$ biologically independent mice; 20 weeks, $n = 4$ biologically independent mice. Saline-treated controls, 10 weeks: $n = 4$; 20 weeks, $n = 4$. Nondiabetic (ND) group: 10 weeks, $n = 4$; 20 weeks, $n = 4$). Error bars represent the standard error of the means (SEM). Statistical comparisons were performed using unpaired two-tailed t-tests. *p < 0.05; **p < 0.01; ***p < 0.001; ****p < 0.0001. Unmentioned group comparisons were considered non-statistically significant (p > 0.05). **h** Pancreas slices from alloxan-treated *Ins2^{CRE}/mTmG* mice were treated with THR-123 for 5 days and then placed on microfluidic chips for continuous monitoring over 72 h, with automated acquisition of all three channels [green, membrane-bound GFP (mG), labeling insulin-expressing cells; red, membrane-bound tomato (mT), labeling non-insulin-expressing cells; and brightfield]. Top row, merge of all three channels at each of the 6 time points. The area in the white tile is shown amplified in the bottom row with only the green (insulin) channel. Dotted-line squares show pre-existing insulin-positive areas that progressively disappear with time. The green arrow observed from the 36 h time point onwards points at a neogenic insulin⁺ area. Size bars: 500 µm. **i** Scheme of the adenovirus-mediated lineage tracing design to study the induction of β-cell neogenesis by THR-123 in slices from non-transgenic (CD-1) mice. mPSs transduced with both AV species feature red non-β-cells and blue pre-existing β-cells. If a non-β-cell (e.g., a ductal cell) generates a β-cell, there will be a transition from red to blue. The transient co-localization of both markers (magenta) is interpreted as β-cell neogenesis. **j** Microphotographs of pancreatic slices co-transduced as indicated in (i) at days 4–9 post-transduction, focusing in a periductal area. Left panel, top row: Blue signal marking cells where activation of the insulin promoter induces a Cre-mediated recombination event leading to the expression of moxBFP. Left panel, middle row: blue and red channels. While on day 4 these two colors largely mark distinct cells (i.e., non-β cells in red, pre-existing β-cells in blue), there is a time-dependent increase of co-localization, indicative of the conversion of non-β-cells into β-cells. Bottom row: brightfield, red and blue channels. Numbered arrows on day 9 point at individual neogenic (magenta) cells. The inset in day 8 shows a single ductal wall cell (number 4) transitioning from red to blue (magenta) as it acquires insulin expression. Size bar: 50 µm. Right panel: Imaging of Ca^{2+} intensity (GMP6) in individual cells (as numbered in the left panel) at day 9 in response to low (3 mM, 3G), high (16.7 mM, 16.7G), second low glucose, and KCl (membrane depolarizing agent). Charts to the right of each cell quantify GcAMP6 intensity throughout the glucose/KCl challenge. Rendering of SliceChip (**h**) was created using Solidworks under a University of Miami license (https://sthd.it.miami.edu/coe/solidworks.pdf). Elements of (**i**) were created in BioRender. DOMINGUEZ-BENDALA, J. (2025) https://BioRender.com/3txycaf).

chip was positioned inside a Keyence microscope/incubator with continuously circulating medium, and Z-stack images of brightfield/red/green channels were taken automatically every 12 h. As shown in Fig. 3h, some residual islets could still be detected (white boxes) but disappeared over time, probably due to a delayed effect of alloxan. However, a new insulin-expressing region appeared around 36 h of THR-123's withdrawal, and its signal (green arrow) persisted until the termination of the experiment. The emergence of new insulin-producing cells as pre-existing ones disappear, observed here for the first time in a live pancreatic tissue, aligns with our interpretation of earlier results, where alloxan/THR-123-treated mice would not become overtly hyperglycemic if new β-cells were formed at the same time as original ones died.

We next sought to determine whether newly formed β-cells were functional by Ca^{2+} imaging[6]. However, as most Ca^{2+} markers emit light in green/red wavelengths, and both are taken in *Ins2^{CRE}/mTmG* mice, we used slices from non-transgenic (CD-1) mice and adapted an adenovirus (AV) co-transduction approach that allows for both insulin expression-dependent tagging and as Ca^{2+} imaging (Fig. 3i). The strategy entails the use of a Rat Insulin Promoter (RIP)-driven Cre lineage tracer (AV1) and a dsRed-to-BFP reporter (AV2). Additionally, the latter features a green GcAMP6s Ca^{2+} marker whose intensity increases proportionally to glucose-stimulated insulin release[6]. In this round of experiments, we tracked the evolution of the dsRed and BFP signals within select ductal areas, rather than the entire slice. The brightfield images of Fig. 3j (left panel, bottom row) show an area of active ductal remodeling within a mPS that was co-transduced and treated with THR-123 for 5 days. There is evidence of the progressive appearance of new BFP⁺ cells as if budding from the duct. These undergo a dsRed-to-BFP transition as the red marker is excised out in cells that express insulin de novo, but where the protein still lingers while the blue marker starts to be expressed (Fig. 3j, lower insets; and Supplementary Fig. 3c). No such transition can happen if a pre-existing β-cell (already BFP⁺) divides. The maximal co-localization between the two markers (magenta) occurs on day 9. We selected 7 cells within this field, all of them in or next to the duct, for Ca^{2+} imaging. Probably due to incomplete maturation, none of these cells showed a complete high-low-high-KCl "canonical" glucose-stimulation response (Fig. 3j, right panel). However, several exhibited a clear reaction to high glucose (1-3, 5-6) or KCl-induced depolarization (1, 4). While our approach is not designed to test whether pre-existing β-cell replication may occur concomitantly, these observations present longitudinal proof of active insulin⁺ cell neogenesis from the ducts, as well as evidence that at least some become partially responsive to glucose. The theoretical alternative that duct-associated β-cells may derive instead from pre-existing islets, as suggested in the TGF-α overexpression model described in ref. 21, is inconsistent with our results. Importantly, these observations could be replicated in pancreatic slices of human origin (Supplementary Fig. 3b), showing that the regenerative effects of THR-123 are conserved across species.

Dynamic scRNAseq of THR-123-treated slices from diabetic mice reveals hybrid ductoacinar cell populations and their transition towards endocrine phenotypes

To further dissect the mechanism through which THR-123 mediates endocrine regeneration, we conducted scRNAseq analysis of pancreatic slices generated from either non-diabetic or alloxan-induced diabetic mice, and cultured for 5 days in the presence or absence of the agent. This length of time was determined based on the maximum functional lifespan of murine pancreatic slices in vitro. Unlike their human counterparts, mouse pancreatic slices are distended with low melting point agarose during their procurement[27]. While this makes

them brittle and difficult to use experimentally after ~5 days in culture, up to that point they provide a solid and anatomically accurate model of a live murine pancreas.

Our experimental approach leverages the integration of scRNA-seq datasets obtained from the same tissue samples (same-donor pancreatic slices), with and without treatment, to conduct a dynamic analysis of regeneration at the single cell level. We hypothesized that treatment of pancreatic slices from diabetic mice with THR-123 may reveal the formation of neogenic β-cells through an intermediate ductoacinar stage, as previously described by our team in human pancreatic slices[6]. While the alternative of conducting these experiments on pancreata harvested from THR-123-treated mice would theoretically enable the analysis of time points significantly more extended than those afforded by the limited functional lifespan of slices in vitro, the dissociation of viable cells (especially acinar) from whole pancreatic tissue remains a major technical hurdle in the field[28]. This is not the case with murine slices, which consistently yield highly viable cells upon dissociation. By providing a more faithful cellular representation of the native organ, our system allows for the dissection of the earliest stages of endocrine cell regeneration with the acceptable tradeoff of having a smaller overall number of endocrine cells.

mPSs ($n = 6$) from non-diabetic mice were thus sequenced after 5 days of culture[5] (positive control). Slices from diabetic mice were either treated with THR-123 (10 nM) for 5 days (experimental group) or left untreated for the same period (alloxan, negative control) prior to sequencing (Fig. 4a). The experiment was repeated three times, and cells pooled for each group. In total, ~32,000 cells were analyzed using the 10X Genomics 5' Single-Cell platform (*Methods*). Libraries were filtered for quality control and subjected to unsupervised clustering, integration and differential gene expression analysis using Seurat v4.1.1 (*Methods*). Differential expression of genes of any given cluster vs. all other clusters was used to identify representative markers. Uniform Manifold Approximation and Projection (UMAP) plots for the positive control (non-diabetic), negative control (alloxan) and experimental group (THR-123) are shown in Fig. 4b–d.

The analysis of control (non-diabetic) slices (Fig. 4b, Supplementary Fig. 4a, b; Supplementary Data 1) revealed ductal (D), acinar (A), endocrine (β- and other cells), endothelial (E), macrophage (M) and mesenchymal-like (MS) clusters. Interestingly, one cluster (H1, *Areg*$^+$) exhibited mixed ductoacinar features. H1 is acinar by position and expression of markers such as *Cela3b* and several cathepsins involved in autophagy and acinar remodeling[29]. However, some cytokeratines (−8, −18, −19) and the ductal progenitor marker *Tff1*[3] are also among the most differentially expressed genes in this cluster, suggesting a hybrid ducto-acinar nature. While mPSs from alloxan-treated mice (negative control) also had ductal and acinar clusters (Fig. 4c, Supplementary Fig. 4c, d; Supplementary Data 2) neither endocrine nor ductoacinar cells were detected therein.

Similar to the positive control, the UMAP of slices from diabetic mice treated in vitro with THR-123 (experimental group; Fig. 4d, Supplementary Fig. 5a, b; Supplementary Data 3) featured endocrine (in smaller proportion) and ductoacinar (in larger proportion) cells. The latter were split between two hybrid clusters, H1 (*Ctse*$^+$) and H2 (*Gm26917*$^+$). In addition to the markers described for the H1 cluster of non-diabetic samples, multiple transcription factors involved in pancreatic development/regeneration were differentially upregulated in these two clusters, including *Sox11*[30], *Klf6*[31], and the triad *Jun*/*Foxq1*/*Sox4*, whose concerted action drives acinar de-differentiation and recovery after injury/inflammation[32]. Other markers in hybrid cells were *2200002D01Rik* (human *C19orf33*), an injury-upregulated factor[33] characteristic of pancreatic progenitors[3,6]; *s100a6*, a calcium-binding protein linked to pancreatic cancer cell motility[34]; *Stmn1*, a cell cycle regulator[35] associated with exocrine progenitors[6]; *Tcim*, a positive regulator of Wnt/β-catenin pathway and Notch signaling inhibitor[36–39]; and the early/immature β-cell markers *Npy* (neuropeptide Y), *Mgst3* (microsomal glutathione S-transferase-3) and *Cldn4* (claudin-4). *Npy* is a co-transmitter detected only in partially differentiated β-cells, only reappearing in mature ones as a result of metabolic stress and/or diabetes[40,41]. *Npy* has been associated to de-differentiated β-cells contributing to compensatory β-cell expansion following partial pancreatectomy[42]. *Mgst3* was originally identified in early β-cells, where it is selectively disallowed as they mature[43,44]. The opposite is true for *Cldn4*, a functional β-cell marker that is progressively upregulated throughout islet development[45]. The single most expressed H1 marker in absolute transcript counts is Clusterin (fourth in H2), encoding a heterodimeric glycoprotein linked to pancreatic regeneration[46–48] (Supplementary Data 4). Most of these markers are also in the equivalent cluster of the non-diabetic control but their expression there is lower (Supplementary Fig. 6). The main difference between H1 and H2 is that the latter is distinctly more pro-endocrine (Fig. 4e). In fact, the most differentially expressed marker in H2 is *Gm26917*, a long non-coding mRNA/insulin transcription activator[49]. Of note, while a recent single-cell atlas of the mouse ductal tree[50] did not report hybrid ductoacinar clusters, that study sequenced only cells expressing Sox9 −a marker with a low level of expression in H1 and H2 (Supplementary Data 4). However, *Fltr3*, a ductal marker with endocrine potential identified therein, does indeed map preferentially in the H1 (higher relative number of cells) and H2 (lower relative number, but higher level of expression) clusters (Supplementary Fig. 3d–e).

Close to H2 is the endocrine cluster (*IAPP*$^+$), absent in the alloxan control (Fig. 4c, e). β-cells are relatively less abundant in this cluster (40.02%) than within its non-diabetic control counterpart (75.17%). They are also less mature, as determined by differential gene expression analysis (Supplementary Data 5) and a Transition Score algorithm (see *Methods*) designed to assess endocrine cell maturity (Fig. 4f).

The makeup and arrangement of the above clusters, alongside the previous data in this work, are consistent with the notion that THR-123 induces β-cell neogenesis in mPSs from diabetic mice, although these cells are still immature (probably due to the relatively short length of the treatment). To test this hypothesis, we combined the alloxan and THR-123 datasets, as the reclustering of the integrated dataset permits an apples-to-apples comparison of the contribution of each group to any given cluster, as well as accurate cell trajectory analyses by dynamic scRNAseq analysis[7] (Fig. 4g, Supplementary Fig. 5c, d; Supplementary Data 6). As before, the combined UMAP features the H1 and H2 hybrid ductoacinar clusters, with the endocrine cells being closest to the latter. Further supporting their potential ontological relationship, a feature plot for *Ins2* shows that H2 (1022 cells) and the endocrine cluster (94 cells) are the only ones with meaningful expression of this marker in the entire dataset (Fig. 4h −inset showing that H2 and endocrine cells are almost entirely derived from THR-123-treated slices).

To further explore this connection and test the hypothesis that endocrine cells arise from H2, we segregated the H2+Endoc clusters from the integrated dataset, subclustered them (Supplementary Data 7), and ran RNA Velocity. By distinguishing unspliced from spliced RNA forms, RNA velocity algorithms such as scVelo[51] can assign pseudotemporal tags (and therefore fate trajectories) to cells in any given dataset[52]. The predictive accuracy of this analysis is greatly enhanced in integrated datasets already containing treatment-dependent information, as the algorithm can more readily 'connect the dots' between cellular stages[6,53]. While H2 is split into three subclusters in the reclustered H2+Endoc UMAP (H2.1-3), the endocrine cluster (*Ppy*$^+$) remains independent, with the exception of 6 (out of 94) endocrine cells that map at the tip of H2.1 (Fig. 4i). We further analyzed this dataset using a suite of RNA velocity tools, namely, scVelo, Latent Time (which offers a representation of any given cell's position along an inferred developmental trajectory), and Partition-based Graph

https://doi.org/10.1038/s41467-025-61534-2

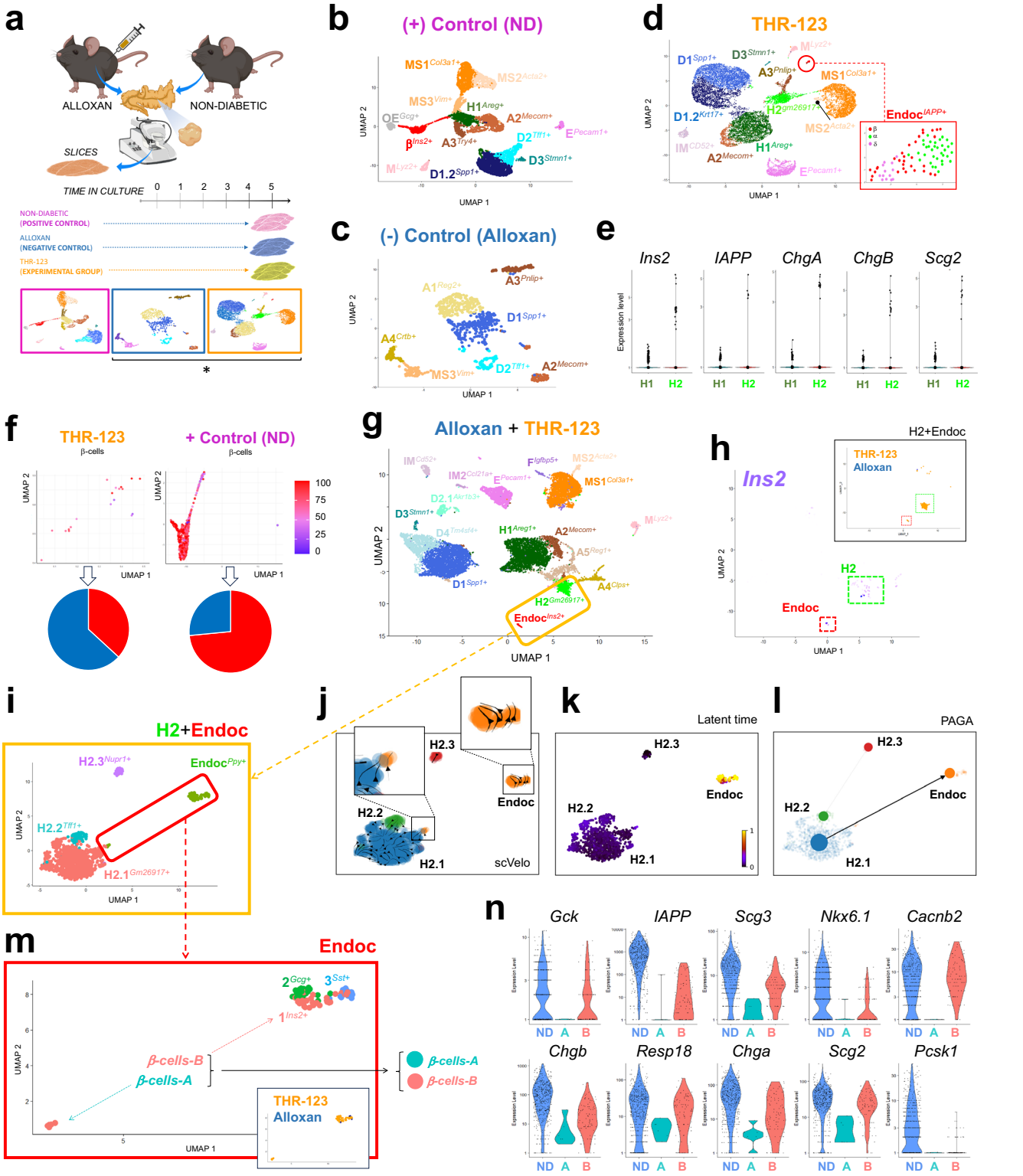

Abstraction (PAGA, which provides visually intuitive directional connections between clusters according to RNA velocity-predictions[54]). These three analyses indicate a fate trajectory from the hybrid ductoacinar cluster H2 to the endocrine one (Fig. 4j–l). Consistent with these results, when we subclustered again the endocrine cells alone (Fig. 4m) we found that all 6 cells identified earlier come from the THR-123 group (Fig. 4m, inset), are β-like (Supplementary Data 8, Fig. 4m), and display lower endocrine maturity than the rest of the cells in that cluster (Fig. 4n).

In summary, even after only 5 days of THR-123 treatment, our study reveals a significant number of immature β-cells (Endoc cluster) that arise from hybrid ductoacinar cells (H2 cluster) as determined by dynamic RNA velocity. Further confirming this transition, the resolution of our analyses is deep enough to detect a handful of cells caught at the very moment of their conversion. The relatively small number of β-cells in our dataset is not considered a limitation, since we ended up detecting the full spectrum of endocrine differentiation from H2 to Endoc. In this context, a higher number of β-cells (as expected if slices

Fig. 4 | Dynamic scRNAseq of mPSs reveals the existence of ductoacinar cells, their activation by THR-123, and the progression of some towards endocrine phenotypes. a Scheme of experimental plan, which entails the generation and culture of mPSs from diabetic (alloxan-treated) and non-diabetic mice and their subsequent culture and dissociation for scRNAseq at day 5. The datasets of alloxan (negative control) and THR-123 (experimental group), as denoted by a bracket and asterisk, were subsequently integrated for RNA velocity analysis. **b** UMAP of positive control (slices from non-diabetic mice). Clusters are classified with a letter based on their main identity (A acinar, D ductal, β- endocrine b-cells, OE other endocrine, M macrophages, E endothelial, MS mesenchymal, H hybrid ducto-acinar) and sub-categorized with a number. To maintain consistency across datasets, a slightly different notation is introduced when two clusters are closely related. For instance, a D1 variation is termed D1.2. Representative markers for each cluster are shown next to their notation. **c** UMAP of negative control (mPSs from mice treated with alloxan). **d** UMAP of experimental group (mPSs from mice treated with alloxan and subsequently cultured in the presence of THR-123). IM: mixed immune cells. Inset: subcluster analysis of the small endocrine (Endoc) cluster, showing three subclusters corresponding to β-, α-, and δ-cells. **e** Relative expression level of endocrine markers in the hybrid ductoacinar clusters H1 and H2. **f** Subcluster analysis of β-cells from the THR-123 group (left) and non-diabetic control (right), in which individual cells have been colored according to their degree of endocrine maturity as calculated by a Transition Score (see "Methods"). Scale: 0 (most ductoacinar, blue)−100 (most endocrine, red). Pie charts represent an average of all the β-cells in each group with a cut-off of 75 (>75, red; <75, blue). **g** UMAP of integrated alloxan (negative control) and THR-123 (experimental group) datasets. F: fibroblasts. The orange box encompasses the hybrid ductoacinar cluster H2 and the endocrine cluster Endoc, which are further dissected by subcluster analysis in (**i**). **h** A feature plot of Ins2 (insulin 2) in the entire integrated UMAP indicates that the expression of this endocrine marker is largely circumscribed to H2 (light green dotted box) and Endoc (red dotted box). The inset additionally shows that the majority of cells in these two clusters originate from the THR-123 group (orange), with only a minimal contribution from the alloxan group (blue). **i** UMAP of the subcluster analysis of H2 + Endoc from the integrated alloxan + THR-123 dataset. While H2 is split into 3 subclusters (H2.1, coral; H2.2, teal; and H2.3, purple), Endoc (Ppy^+, green) remains as an independent cluster. However, there are several cells from Endoc at the rightmost tip of H2.1. RNA velocity analyses were performed on this integrated dataset. **j** scVelo distinctly shows outgoing fate trajectory arrows from the Endoc cells at the tip of H2.1 (left inset) and incoming arrows in the main Endoc subcluster. **k** Latent time analysis indicates that cells in H2.1 are at the origin and main Endoc cluster cells at the destination [color scale from black (0) to yellow (1) indicating starting and ending RNA velocity stages]. **l** PAGA (PArtition-based Graph Abstraction) analysis further confirms an H2.1 to Endoc direction of transition. **m** Additional subclustering of the endocrine cells confirms that the 6 cells at the tip of the hybrid ductoacinar subcluster H2.1 are β-like, although most β-cells (subcluster 1) are located in the main endocrine cluster alongside α- (subcluster 2) and δ- (subcluster 3) cells. We termed the 6 endocrine cells in the ductoacinar location β-cells-A and the ones in the main Endoc subcluster β-cells-B. The inset shows that all 6 β-cells-A are from the THR-123 group (orange). **n** Violin plots of select endocrine markers confirm that β-cells-A (teal) are less mature than β-cells-B (coral), further supporting the notion that they represent a transitional stage from the ductoacinar cluster. Relative expression levels of the same markers in β-cells from non-diabetic control samples are also shown as a reference. Elements of panel 4a were created in BioRender. DOMINGUEZ-BENDALA, J. (2025) https://BioRender.com/3txycaf.

could be pushed to survive for longer, thus allowing for further differentiation) would not have changed the conclusions of our analysis or made them any stronger.

Of note, the dynamic scRNAseq analysis of the Endoc cluster does not reveal any proliferative signature in these immature β-cells (Supplementary Data 5 and Supplementary Fig. 3f, g), suggesting that the division of pre-existing β-cells is not the predominant mechanism through which THR-123 exerts its action. Our conclusion that new β-cells arise from specific ductal cell subpopulations in this experimental setting is strongly aligned with all the preceding results described in this work.

Discussion

We demonstrate that THR-123, a BMPR agonist, drastically reduces hyperglycemia in diabetic mice. While our data do not entirely discard that THR-123 may also impart protection to islets and/or reduce inflammation, the body of our research points at β-cell neogenesis as the primary effector of this experimental outcome. BrdU incorporation assays already confirm de novo formation of functional islets, but our studies go one step further by leveraging the pancreatic slice platform[3,6,53,55] to both visualize β-cell formation in real time and dissect the transcriptomic dynamics of the process at the single cell level.

The latter studies suggest that THR-123 induces the transition of pre-existing hybrid ductoacinar cells towards endocrine phenotypes. The involvement of an intermediate ductoacinar-like stage is an emerging concept in the field first posited by our team following the dynamic scRNAseq analysis of HPSs exposed to BMP-7[6]. Shortly afterwards, another team independently described a hybrid population of peri-islet acinar cells with the ability to become β-cells in mice[24]. This is the first report describing in detail the entire ductoacinar-endocrine regeneration arch in a live diabetes model. We discovered a highly plastic, differentiation-ready population of cells with hybrid ductoacinar features in the normal pancreas (cluster H1). Following the induction of diabetes and the treatment of slices with THR-123, our analyses reveal the relative expansion of this cluster, the accentuation of its stemness, the formation of a related cluster (H2) with pro-endocrine characteristics, and, finally, the presence of a cluster of β-cells of immature characteristics. The application of RNA velocity tools indicates that the latter arises from H2 and not the other way around. Our approach was powerful enough to capture a snapshot of the active process, i.e., the transcriptome of a handful of cells at the very moment of their transition (see "Results"). This study suggests that factors such as *Klf6*, *Sox4/9*, *Jun*, *Foxq1*, *Stmn1*, *Tcim*, *Npy*, *Mgst3*, *Cldn4*, and *Clu* –all previously linked to regenerative processes in the pancreas– may be critically involved downstream BMPR activation. Whether the selective conditional inactivation of these molecular players impairs the THR-123-dependent induction of β-regeneration will be the subject of future studies.

It is important to emphasize that the conclusions of our work do not solely rely on scRNAseq trajectory predictions but are bolstered by a comprehensive array of experimental approaches. Chief amongst them is the lineage tracing of neogenic insulin-expressing cells transitioning from the ducts, a pivotal piece of evidence supporting the progenitor cell hypothesis of regeneration[16]. While a small degree of co-localization between Alk3 and insulin staining in THR-123-treated mice already suggested this transition (see "Results"), these static snapshots (the last in a long list of historic observations of islets ostensibly sprouting from ducts[16,56,57]) are insufficient to prove that this phenomenon may occur dynamically[58] under specific circumstances. The real-time monitoring of ductal cells in their native anatomical context as they adopt an endocrine phenotype is a technical breakthrough that has eluded researchers for decades, and a prime example of the power of the pancreatic slice model[5,26,53,55].

Aligned with the principle of in vivo *veritas*, experiments with diabetic mice additionally confirm that THR-123 induces the formation of new islets with average BrdU labeling rates in excess of 60% –percentages that may underrepresent the actual rate of β-cell neogenesis owing to the low bioavailability of BrdU[59], dilution in rapidly dividing cells over time[60], low detection sensitivity[61], and the maximum length of treatment (6 weeks) recommended to minimize toxicity. These percentages also account for the fact that BrdU quantification includes islets that are nearly 100% labeled alongside smaller, possibly residual ones that have no BrdU label. Importantly, while our observations cannot rule out the subsequent self-expansion of β-cells after they form (as proposed in ref. 57), or that THR-123 may also have a direct effect on the proliferation of pre-existing β-cells, multiple lines

of evidence argue against self-replication as the main mechanism behind our observations: First, BrdU incorporation levels are similarly high in ducts as they are in islets, indicating that this is not a β-cell-specific effect. Second, β-cells do not proliferate in response to BMP signaling[1,14], and, in fact, other groups have shown that BMPs inhibit β-cell growth[62]. Third, the differential presence of extensive ductal networks within islets of THR-123-treated mice suggests either active or vestigial regeneration foci (e.g., ducts trapped within the islets they gave rise to). Intrainsular ducts exist in normal islets[22] but to a much lower extent (see "Results"). This observation has not been reported for islets regenerated through self-replication[13]. While absence of evidence is not evidence of absence, it would be difficult to explain why the self-replication of β-cells alone (which BMP signaling does not induce in any case) would lead to the growth of these intrainsular ductal networks. Fourth, we have already determined that ALK3 (not expressed in β-cells) is the most likely BMP receptor mediating the effect of BMP signaling in the human pancreas[14], which we subsequently confirmed by lineage tracing in vitro[1]. Fifth, we present real-time evidence of insulin$^+$ cell expansion (BFP$^+$) from ducts in live pancreatic slices. These cells undergo an intermediate dsRed-to-BFP stage, which would never be seen if pre-existing β-cells were merely self-replicating. This observation is additionally supported by our finding of Alk3 and insulin co-localization upon THR-123 treatment, an occurrence that was specifically ruled out in other regeneration models that propose an islet origin for the β-cells that line ducts[21]. Finally, our dynamic scRNAseq analyses (including the conspicuous absence of a proliferative signature in THR-123-induced β-cells), and, above all, the collective learnings from our previous body of work on this model[1,3,5,6,14,16,53], paint together a picture consistent with a ductal-only origin for the newly created β-cells that we report on THR-123-treated animals.

Open questions about the basic processes governing ductal-mediated regeneration include: (a) whether neogenesis and delamination may be followed by a progressive coalescence and/or proliferation of endocrine cells; (b) the nature of the local environmental milieu that dictates whether stimulated progenitors differentiate along one lineage or another; and (c) the study of factors affecting the preferential activity of BMPR agonists in the diabetic pancreas vs. other organs. Planned long-term studies (e.g., by conducting spatial transcriptomics of biological samples with evidence of regenerative remodeling and transplanting pancreatic slices in the anterior chamber of the eye for long-term longitudinal follow-up of these events) will shed additional light on these important questions.

From a therapeutic perspective, the engagement of the BMP pathway has been linked to regeneration in multiple disease models[7,8,63,64]. BMP-7 itself, the primary BMPR agonist used in our previous work on endocrine regeneration[1,5,6,14], has been approved for the treatment of bone repair for over two decades[65]. The activation of resident pancreatic progenitor-like cells by pharmacological means would be of utmost significance to develop combination therapies for insulin-dependent diabetes. The agent employed in this study, THR-123, has been shown to have cardioprotective myocardial remodeling effects[8] and reverse kidney fibrosis in mice[7]. Reservations about potential off-target induction of proliferation are not particularly concerning from a clinical perspective, provided that there is a therapeutic effect and higher cell division rates are restricted to progenitor niches during exposure to the drug. In fact, proliferation is not considered an impediment at early drug development[66], and the FDA has approved many drugs with non-specific proliferative effects, such as estrogen or human growth hormone. At any rate, off-target increases of basal proliferation rates could not be detected either in non-diabetic mice or in the extrapancreatic tissues of diabetic mice exposed to THR-123 (see "Results"). These findings suggest that an insult (e.g., alloxan) may be needed for THR-123 to exert its action, and chiefly at the injury site[16,67]. THR-184[8,9], a sister molecule of THR-123, has completed a multicenter Phase 2 clinical trial for acute kidney injury following cardiac surgery. While the study was discontinued after Phase 2 due to partial lack of efficacy for the intended application, the agent was given systemically to hundreds of subjects with no toxicity or meaningful side effects[10]. No information about potential metabolic effects of the drug in these patients is available.

Along with other promising approaches aimed at inducing endogenous regeneration[24,68–70], small-peptide BMP mimetics could be used as a clinical alternative to cell products (isolated[71,72] or stem cell-derived[73] islets) to restore β-cell mass in situ without the rigors and limitations of transplantation. The action of BMP signaling on the ductal tree of murine and human pancreata has been characterized in depth and the responsive populations resolved at the single-cell level[1,3,5,6,14].

Limitations of our study include mouse-to-mouse variability (e.g., in responses to alloxan or recovery rate). While inherent to all animal studies, this may have been exacerbated by the use of the outbred line CD-1. However, owing to its greater genetic diversity compared to inbred strains, basing the bulk of our experiments on this model also increases the robustness of our results. Another potential drawback of our research is that in vitro lineage tracing designs may be affected by epigenetic modifications of the AV-carried transgenes and/or regulatory sequences[74]. This could lead to unpredictable inactivation or reactivation (e.g., of the transgenic insulin promoter) depending on the cellular environment or external stimuli affecting the cell's epigenetic landscape. Also, the expression of the Ins2 promoter has been shown to change dynamically according to β-cell maturity stages[75]. Additional lineage tracing analyses based on the use of ductal-specific drivers may complement and reinforce our conclusions, but the reliability of promoters such as Hes1, HNF-1β or Sox9 is also suboptimal due to variable temporal expression patterns (especially in replicative cells) (rev. in ref. 76). While no lineage tracing approach is faultless, it is important to emphasize that this is only one of the many orthogonal approaches that collectively inform our conclusions. Finally, whether our results in mice can be translated to humans is an open question. However, our data suggest a high degree of interspecific conservation of this regenerative pathway. Taken together, the efficacy of BMPR agonists in HPSs from non-diabetic and type 1 diabetic donors[6], the sustained endurance of BMP-sensitive cells in the pancreas of diabetic patients[3], and the favorable safety profile of BMPR agonists[64] strongly support the pharmacological development and clinical use of THR peptides to treat insulin-dependent diabetes.

Methods

Experimental animals

All animal experiments were conducted under the supervision and oversight of the Institutional Animal Care and Use Committee (IACUC) and Division of Veterinary Resources (DVR) at the University of Miami. For all experiments, mice were acclimated for 7–10 days prior to any experimental intervention. They were maintained on a 12 h light/dark cycle with *ad libitum* access to standard irradiated chow and filtered drinking water. CD1 mice: CD1-IGS mice (5–6 weeks old; Charles River, Wilmington, MA, Cat# 022) were utilized for most in vivo and in vitro experiments. Due to the widely reported challenge of consistently inducing diabetes in female mice through chemical means[77–79], we used male mice to test our hypothesis.

THR-123 biodistribution. THR-123 (LT-1090-11, LifeTein) was labeled with Fluorescein amidites (FAM), which imparts green fluorescence. FAM-labeled THR-123 was given to CD1 mice by intraperitoneal (i.p.) injection (6.25 mg/kg). After 2hrs and 5 hrs. of injection, animals were euthanized and the tissues collected and immediately embedded in Tissue Embedding Medium Tissue-Tek Cryo-OCT Optimum Cutting Temperature (OCT) Compound Clear Liquid. (McKesson MPN MPSMK-649078). Frozen sections of 5 μm were imaged ApoTome Axiovert 200 M (Zeiss) fluorescent microscope.

THR-123 treatment of diabetic mice. Male CD1 mice or C57BL/6 of 6–8 weeks of age were fasted for 12 h and rendered diabetic by either a single injection of 150 mg/kg of Alloxan monohydrate (Sigma Aldrich A7413, CAS Number: 2244-11-3), up to three injections of alloxan (70 mg/kg), or five injections of streptozotocin (*stz*; 40 mg/kg). Two settings were explored: One where mice were randomized and THR-123 initiated at the same time as the chemical induction of diabetes and another where diabetes was induced first and then mice with three consecutive blood glucose (BG) measurements above 250 mg/dL were randomized, assigned to the experimental groups, and treated with THR-123 by *i.p.* injection. Controls received saline injections with the same frequency. Glycemia was monitored at variable frequencies (typically daily or twice a week for short-term experiments; longer intervals after 10 weeks for long-term experiments). Upon euthanasia, the pancreas, brown fat and peripheral blood were harvested from select animals. Intraperitoneal glucose Tolerance Tests (IPGTTs) were done at specific time points, and blood samples collected to measure circulating C-Peptide, insulin, and glucose. All metabolic analyses were performed on healthy, conscious and restrained mice on the days indicated in the manuscript. Peripheral blood was obtained via saphenous vein and tested for glucose using a handheld glucometer (Bayer, Whippany, NJ). Blood samples were collected in heparinized microhematocrit tubes. Plasma was separated by centrifuging samples at 2400 rpm for 10–15 min. Collected plasma was frozen at −20 °C. Concentrations of IL6, IL10, IL17A, TNFα and MCP-1 were assessed using the Luminex Discovery assay from (Bio-Techne-R&D Systems). Mouse C-peptide ELISA (APLCO Cat#: 80-COPMS-E01) and Mercodia Mouse Insulin (cat #10-1247-01) were measured according to the manufacturer's recommendations. For IPGTTs, mice were fasted for 6 h prior to administration of a 2 g/kg BW glucose bolus. Blood was collected prior to the administration of the bolus and after 60 min. At the termination of the experiment, mice were sacrificed, and pancreas, kidneys, liver and lungs extracted and preserved in 10% paraformaldehyde for histological immunofluorescence imaging analysis. Brown fat was collected, weighed, and preserved in RNA/later stabilization solution (Thermo Scientific, cat#: AM7020).

BrdU. To study cumulative cell proliferation, 5-Bromo-2′-deoxyuridine (BrdU) (Sigma Aldrich B5002, CAS number: 59-14-3) was added into the drinking water (0.8 mg/mL) for up to 6 weeks.

Ins2-Cre/mTmG mice. In order to create the *Ins2-Cre/mTmG* transgenic line, we crossed B6.Cg-Tg(Ins2-Cre)25Mgn/J (INS2-Cre; Jackson Labs, Bar Harbor, ME, Cat# 003573) with B6.Gt(ROSA)26Sortm4(ACTB-tdTomato,-EGFP)Luo/J (mTmG; Jackson Labs, Bar Harbor, ME, Cat# 007676). In the resulting mouse, all insulin-producing cells express fluorescent membrane-bound EGFP, while all non-insulin-producing cells express fluorescent membrane-bound tdTomato. We used only F1 generation mice for β-cell regeneration experiments. Stability of the mTmG mouse was gauged by culturing mTmG slices from both male and female mice and examining fluorescence patterns.

Calculation of insulin sensitivity. To determine insulin sensitivity in mice, we use the Matsuda Index, calculated with the following formula:

$$\text{Matsuda Index} = 10000 / \sqrt{[(Go*Io)|(Gm*Im)]}$$

where:

G_0: Fasting glucose concentration

I_0: Fasting insulin concentration in μU/mL

G_m: Mean glucose concentration during IPGTT

I_m: Mean insulin concentration during IPGTT in μU/mL

This formula provides an assessment of insulin sensitivity based on glucose and insulin levels measured during an oral or intraperitoneal glucose tolerance test. Mice with normal insulin sensitivity are expected to have indices above 4.0[80].

Mouse pancreatic slices (MPSs)

Generation. MPSs were generated from either CD1 or *Ins2-Cre/mTmG* mice based on methods described in ref. 81. To facilitate slicing of the rodent pancreas, the tissue was hardened prior to extraction by intraductal injection of 1.5% low-melting point agarose (Agarose, Low Melting Point, Cat. No. V2111, Promega). The agarose was melted and maintained at 37 °C before use. Animals were euthanized by cervical dislocation, and the abdominal cavity was opened to expose the hepatopancreatic region. The ampulla of Vater was clamped, and 1–2 mL of 1.5% agarose injected retrogradely through the common bile duct, allowing it to flow into the pancreatic ductal system. To enhance tissue firmness, ice-cold HEPES buffer was applied to the surface of the pancreas. Once adequately hardened, the pancreas was carefully excised from the abdominal cavity and transferred to a fresh dish containing ice-cold HEPES buffer for washing. The tissue was then dissected along the ductal axis into smaller pieces. These tissue fragments were placed in a 35-mm dish and embedded in freshly prepared 1.5% low-melting point agarose at 37 °C. The embedded samples were immediately cooled on ice to solidify. A small agarose block containing the pancreas was cut from the dish and affixed to the specimen stage of a vibratome (e.g., VT1200S, Leica Biosystems). The vibratome chamber was filled with ice-cold HEPES buffer, and slicing was performed at a speed of 0.1 mm/s, an amplitude of 1 mm, and a section thickness of 120 μm. Slices were collected gently using a fine brush and transferred into chilled HEPES buffer for brief equilibration prior to downstream culture steps, as described below.

Culture. Murine slices were cultured in uncoated AirHive® dishes made to order by Biorep, Miami, FL in customized Waymouth's MB 752/1 medium (with L-glutamine; without D-glucose; Biological Industries, Cromwell, CT, Cat# 06-1110-01-1A) supplemented with 11 mM D-glucose (Sigma Aldrich, St. Louis, MO, Cat# G8644), 1% heat-inactivated FBS (Invitrogen, Carlsbad, CA, Cat# 16140063), 100 μg ml−1 trypsin inhibitor from Glycine max (Sigma Aldrich, St. Louis, MO, Cat# T6522), 10 μg ml−1 aprotinin (Sigma Aldrich, St. Louis, MO, Cat# A6106), 10 μg ml−1 chymostatin (solubilized initially in DMSO; Sigma Aldrich, St. Louis, MO, Cat# 11004638001), and 1× penicillin–streptomycin–amphotericin B solution (Sigma Aldrich, St. Louis, MO, Cat# A5955). Dishes containing slices (maximum 2) and medium (maximum 2 ml) were placed in a humidified incubator at 30 °C for up to 10 days. Medium was changed daily.

Adenoviral vector transduction. Recombinant adenoviruses (AVs) were constructed using the serotype 5 adenovirus with an E1/E3 deletion. A codon-optimized Cre variant was used. The lineage tracer was cloned upstream of a codon optimized Cre to create an Adv-RIP-Cre adenovirus. The reporter construct was loaded onto an adenoviral packaging plasmid to create the Adv-(CMV)-LoxP-dsRED-LoxP-moxBFP-2A-GCaMP6s adenoviral reporter. All adenoviral construction was performed at Vector Biolabs (Malvern, PA, USA). Slices were transduced with a Multiplicity of infection (MOI) of 50 for the reporter and a MOI of 10 for the lineage tracer. AVs were stored at −80 °C. Once thawed, the virus was diluted in 0.1 μl/ml of Waymouth medium and then filtered using a 50 ml 0.22 μm filter. The medium was then removed from the dishes covering the murine pancreatic slices. 2 ml from the virus preparation was added into each dish and incubated at 30 °C for 24 h. The next day, the virus was removed by pipetting or vacuuming. 1 ml of Waymouth medium was added to each dish for 5 min to wash the slices. After removal, treatment was started as indicated with medium + THR-123 (LifeTein LLC, Somerset, NJ, USA).

Live imaging analysis of MPSs in AirHive® dishes and microfluidic chips. Prior to treatment, THR-123 (LifeTein LLC, Somerset, NJ, USA) was dissolved in PBS (PBS pH 7.4 (1X), Cat# 10010-0232, Gibco) to a final concentration of 10 μM and stored in aliquots at −80 °C. To treat MPSs, an aliquot was removed and thawed on ice. Once thawed, THR-123 was further diluted by adding 1 μL of the suspension to 1 mL of medium, bringing the final concentration of THR-123 to 10 nM. MPSs

received this treatment for 5 days in AirHive® dishes starting at the same time of transduction. Medium was changed daily (typically with THR-123 for 5 days and without it for the following 5 days) and slices imaged also daily at 4x (to capture most of the slice) and 20× in specific regions of interest (ROI) that were arbitrarily selected on the first day of treatment using topographical landmarks present in the slice to ensure accurate longitudinal imaging. Images were captured in brightfield, red and blue channels. Blue (moxBFP) signal corresponding to pre-existing β-cells in the MPSs can be typically observed soon after transduction. These cells do not exhibit red fluorescence at any point. Neogenic insulin-producing cells (observed mostly after the removal of THR-123 in the experimental group) are dsRED-labeled cells that at some point of the treatment also start expressing moxBFP, reflecting a late recombination event resulting from the new onset of insulin expression. An alternative setup is one where slices from *Ins2-Cre/mTmG* mice were treated with THR-123 in vitro (AirHive dishes) for 5 days and then placed within a customized SliceChip for A 72h-period time-lapse fluorescence imaging (red, green and brightfield channels). During this time, slices were perfused with media at 80 µl min−1 and imaged every 12 h within a Keyence BZ-X810 all-in-one fluorescent microscope with a Z-stack height of 105–120 and step height of 5–15 across a 32–40-tile grid. Post-acquisition, a full focus stitch of the Z-stack and tiles was generated using the built-in z-stack and stitching functions of the microscope. Slices are examined with fluorescent microscope daily.

SliceChip Setup. A complete, stepwise protocol is described in ref. 26, a brief overview of which is included here. All components of the system were sterilized prior to use. Fluidic tubing, bubble traps, analytical selector valves, degassing chambers, flow units, and the microfluidic chip were sequentially flushed with 70% ethanol, sterile distilled water, and dried with clean air. Media bottles, GL-45 caps, Micronit clamps and ferrules, pneumatic tubing, and all associated connectors were autoclaved using a 60-min gravity cycle. In addition, all parts were exposed to UV light for 30 min for surface sterilization. Following sterilization, media bottles were filled with pre-warmed culture media, sealed with GL-45 pressure caps, and connected to the analytical selector valve. The tubing was connected in the following order: degassing chamber → bubble trap → Micronit clamp → flow units. Once the fluidic pathway was fully assembled, tissue slices were positioned at the base of the microfluidic chip and immobilized using a custom 3D-printed stainless steel (316L) slice anchor. After centering and securing the slice, the top layer of the chip was aligned and sealed using the clamp system. The assembled SliceChip was then placed onto a Tokai Hit incubation stage set to maintain a temperature of 37 °C and positioned within a Keyence inverted fluorescence microscope. Media reservoirs were connected to a pressure pump and submerged in a bead bath to ensure temperature stability.

Ca^{2+} imaging. In ex vivo-treated mPSs that were previously infected with an AV-RIP-Cre tracer and an AV-(CMV)-LoxP-dsRED-LoxP-BFP-2A-GCaMP6s reporter, expression of GCaMP6s allows for the study of the functionality of insulin-producing cells (moxBFP$^+$ arising from cells with previous dsRED expression) by measuring the accumulation of cytosolic Ca^{2+} in response to glucose stimulation. To this end, we connected the VCS Valve Control System (Warner Instruments, Holliston, MA) to a Keyence BZ-X810 all-in-one-microscope using the time-lapse module (BZ-H4XT #5J120010). GcAMP6s imaging (green channel) was done with a 20X objective on areas where neogenic insulin-producing cells were identified on any given ROI. Before imaging, slices were stabilized for 1 h in 3 mM glucose solution. 8 ½ images were taken per minute (every 7 s). The total imaging time was 63 min. For the first 3 min, slices were bathed in medium with 3 mM glucose, followed by 16.7 mM glucose stimulation (20 min). MPSs were taken back to baseline levels (3 mM glucose) for another 20 min, and finally stimulated with 30 mM KCl for 20 min. The flow rate of the system was maintained constant throughout the course of the experiment (100 µl/min). Acquired images were reconstructed in Z-stacks of 7–8 confocal images (step size = 12 µm) by the Keyence Analyzer software in an.avi format and played at 5 frames per second. GcAMP6s fluorescence intensity was measured using the ImageJ/FIJI imaging analysis program. Changes in fluorescence intensity are expressed as percentage changes over baseline (ΔF/F). We measured changes in GcAMP6s intensity by graphing the area under the curve above baseline using Prism (Prism 9, GraphPad software, La Jolla, CA). Our criteria for accepting intracellular Ca^{2+} ($[Ca^{2+}]i$) responses for graphing were that: (1) responses could be elicited ≥2× by the same stimulus; and (2) the peak signal was ≥2 times the baseline fluctuation. We selected cells that responded to increases in $[Ca^{2+}]i$ during KCl and high glucose (16.7 mM) stimulation.

Immunostaining and imaging quantification

Mouse Pancreatic Slices. Tissue slices were washed 3× for 15 min in 1× phosphate buffered saline (PBS), pH 7.4 (Sigma Aldrich, St. Louis, MO, USA Cat# P3813), and fixed in 4% paraformaldehyde solution (Paraformaldehyde 32% Solution, EM Grade, Cat# 15714, Electron Microscopy Sciences) for 1 h. Slices were then washed 7× for 10 min in 1× phosphate buffered saline (PBS), pH 7.4 (Sigma Aldrich, St. Louis, MO, USA Cat# P3813). Permeabilization was done for 60 min using 0.3% Triton (Sigma Aldrich, St. Louis, MO, USA Cat# T9284-500 ml) in 1× PBS, pH 7.4 (Sigma Aldrich, St. Louis, MO, USA Cat# P3813). After this, slices were placed in a blocking buffer containing dH_2O, 5% normal donkey serum (Jackson Labs, Bar Harbor, ME, Cat# H-400), 0.1% Triton, and 1× power block (Biogenex, San Ramon, CA, Cat# HK0855K). Primary antibodies were dissolved in the blocking buffer and incubated for 48 h at 4 °C. They were subsequently removed, and slices washed 7× for 10 min with 1× PBS, pH 7.4/0.1% Triton. Secondary antibody solutions (1:400) were made with Alexa Fluor 488, 594 or 647 donkey anti-primary antibody species and 1:800 4′, 6-diamidino-2-phenylindole (DAPI) (Thermo Fisher/Life Technologies, Waltham, MA, Cat# D1306) in blocking buffer. Slices were incubated with secondary antibodies overnight and then washed 12× for 10 min with 1× PBS, pH 7.4. To get the least amount of background fluorescence, an additional wash was performed overnight at 4 °C with 1× PBS, pH 7.4. For imaging, slices were mounted on crystal slides (Staining Kit, Arcturus, Cat# Kit0420) with ProLong mounting reagent (ProLong Gold antifade reagent, Invitrogen, Cat# P36934) and sealed with a cover slip (Micor cover glass, VWR, Cat# 48393). Imaging was acquired using a Keyence BZ-X810 fluorescent microscope. Z-stack depth ranged between 120–130 µm depending on the slice thickness and condition while the number of images in the Z-stack ranged between 15–25 with a step size ranging between 2.5–4 µm.

Tissue sections. Paraffin-embedded slides were taken from the 4 °C storage refrigerator and adjusted to room temperature (RT). Deparaffinization of the slides was performed using an Autostainer XL (Leica Biosystems, Wetzlar, Germany, Cat# ST5010) programmed for 3 × 2 min dips in xylene, 2 × 1-min dips in absolute ethanol, 1 × 30 s dip in 95% ethanol, 1 × 45 s dip in 70% ethanol, and a final wash in dH_2O. Antigen retrieval was performed by submerging the slides of murine pancreatic tissue in antigen decloaker at pH 6.0 (BioCare Medical, Pacheco, CA, Cat# CB910M). The slides with the decloaker solutions were then placed inside a Decloaking Chamber Pro (BioCare Medical, Pacheco, CA, Cat# DC2012) for 10 min at 120 °C and then cooled down to RT. Slides were then washed 2× for 5 min in 1X phosphate buffered saline (PBS), pH 7.4 (Sigma Aldrich, St. Louis, MO, USA Cat# P3813), and 1x for 5 min with dH2O. For permeabilization, we added 0.3% Triton (Sigma Aldrich, St. Louis, MO, USA Cat# T9284-500-ml) to 1× PBS, pH 7.4. To apply this buffer, a hydrophobic edge was drawn on the glass slides around the tissue section using the ImmEdge Pen (Vector laboratories Burlingame, CA, Cat# H4000). Permeabilization buffer, were placed on the tissue section within the edge. After 30 min, the permeabilization buffer was replaced by blocking buffer containing

[dH_2O, 5% normal donkey serum (Jackson Labs, Bar Harbor, ME, Cat# H-400), 0.1% Triton and 1× power block (Biogenex, San Ramon, CA, Cat# HK0855K)]. After 1 h, an additional blocking step was done for 10 min with serum-free protein block (Dako, now Agilent, Santa Clara, CA, Cat# X0909). Primary antibodies were dissolved in the blocking buffer and incubated overnight at 4 °C. Primary antibodies were then removed, and sections washed 7× for 5 min with 1× PBS, pH 7.4/0.1% Triton. Secondary antibody solutions (1:400) were made with Alexa Fluor 488, 594 or 647 donkey anti-primary host antibody and 1:800 4′, 6-diamidino-2-phenylindole (DAPI) (Thermo Fisher/Life Technologies, Waltham, MA, Cat# D1306) in blocking buffer. Samples were incubated with secondary antibodies for 60 min and then washed 7× for 5 min with 1× PBS, pH 7.4. To get the least amount of background fluorescence, an additional wash was performed overnight at 4 °C with 1× PBS, pH 7.4. After the last washing step, a drop of Prolong™ Gold Antifade solution (Thermo Fisher, Waltham, MA, Cat# P36930) was added and the sections protected with Micro cover glass (VWR, Radnor, PA Cat# 48393-081) and sealed with clear nail polish. (INM, Anaheim, CA, Cat# S401025).

Imaging quantification. Sections from the different experimental groups were imaged and analyzed. From each section, three images at 20x magnification (4 channels each: DAPI, FITC, TRIT CUBE & CY5), were taken using a scanner in the Olympus VS120 with Hamamatsu Orca Flash 4.0 sCMOS fluorescence camera or Leica Stellaris 5 confocal microscope. We used the cell counter plug-in from ImageJ/FIJI software (NIH) to count cells of specific phenotypes. From every image, DAPI-positive cells were counted to determine the total number of cells, against which all the other markers were quantified. Statistical analyses were done using GraphPad Prism v8. For image analysis, we used FIJI-ImageJ software (Version 2.1.0, National Institutes of Health, USA) to examine multi-channel fluorescence images. To streamline the handling of extensive image files, we incorporated bespoke macro scripts into the software, including a macro that automates the integration of DAPI, BrdU, CK7, and insulin-stained photos into a single composite file. We then applied machine learning-based segmentation with the Weka segmentation plugin to quantitatively analyze cellular markers. Using a pre-trained classifier, we categorized and measured the presence of insulin and BrdU-positive cells and quantified CK7 expression and MFI. Image J analysis codes for the above operations can be accessed as indicated in the Code Availability section. Islet regions were identified by the presence of insulin, and the MFI of CK7 was quantified in these areas using ImageJ's integrated density function. The data were preserved and summarized for subsequent statistical analysis. The results were analyzed using pairwise group comparisons, we systematically used a non-parametric statistical test (unpaired, two-tailed Mann-Whitney test) and Wilkinson (test for non-parametric rank). The p value significance threshold was defined as 0.05. Finally, graphs were made with GraphPad Prism v8.

Mouse islets and non-endocrine pancreatic tissue

Perifusion of mouse islets. From mouse islet isolations conducted in-house by the Translational Models Core, 10 K IEQ were spun after washing in RPMI media at 100G for 5 min and resuspended in 1 mL. 100 µl were used for perifusion for each group using a PERI4 machine (Biorep Technologies, Miami, FL, USA), allowing to run all three conditions in parallel. For each experiment, 100 mouse IEQ were loaded into microcolumns and embedded within two layers of acrylamide-based microbeads (Bio-Gel P-4, Bio-Rad Laboratories, Hercules, CA, USA). The perifusion buffer contained 125 mM NaCl, 5.9 mM KCl, 1.28 mM $CaCl_2$, 1.2 mM $MgCl_2$, 25 mM HEPES, and 0.1% bovine serum albumin, adjusted at pH 7.4. Islets were perifused at 37 °C using different glucose concentrations or KCl (25 mM) at a rate of 100 µL/min. Equilibration was performed for 60 min using 3 mM glucose and eluates were collected every minute thereafter. Islets were stimulated with the following sequence: 8 min of 3 mM glucose, 20 min of 16.7 mM glucose, 15 min of 3 mM glucose, 10 min of 25 mM KCl, and 10 min of 3 mM glucose. Insulin concentrations were determined using a commercially available mouse insulin ELISA kit (Mercodia Inc., Winston Salem, NC, USA) following manufacturer instructions. Data were normalized by DNA content (PicoGreen).

Apoptosis assay. Following the treatment, 100 IEQ per group were collected, washed in PBS, fixed in PFA 4% for 30 min, and embedded in Tissue-Tek® O.C.T. Compound (Sakura Products, cat# 4583). Sections of 5 µm were obtained and processed. Tissue sections were taken from the −80 °C storage and adjusted to room temperature (RT). Permeabilization was performed as described in the immunostaining section. Islets were stained with Cleaved Caspase-3 (Asp175, Cell Signaling cat# 9661), insulin (Dako A0564), and DAPI. Sections were imaged using an Apotome Axiovert 200 M (Zeiss) fluorescent microscope.

Flow cytometry of mouse non-endocrine pancreatic tissue. Cells were harvested, filtered and stained in DPBS with the viability dye eFluor 780 (eBiosciences/ThermoFisher) for 15 min at 4 °C in darkness. Cells were then washed 3 times using DPBS and then fixed with DPBS + 10% formalin. Subsequently, they were incubated in blocking buffer for 1 h. After 3 more washes, the cells were stained in blocking buffer with 1:50 anti HNF1β, Proteintech, (Cat. # 125331AP). Following 3 additional washes, they were counterstained with anti-Rabbit-A594 (Thermo Scientific), incubated for 30 min away from light at room temperature, washed 3 times, and resuspended in re-suspension buffer. This was followed by the incubation of 2 µL of anti-SOX9 (Bioss, cat# bs4177R-A488), anti-CD24-450 (Invitrogen cat# 48-0242-82), anti-BMPR1A-A647 (Bioss cat# bs1509R-A647), anti-P2Y1R-FITC (Biorbyt), and anti-pSmad PE (Cell Signaling 13820S) per tube, 45 min away from light at room temperature. After three consecutive washes, cells were then resuspended in Flow Cytometry Staining Buffer (500 µl) and analyzed by flow cytometer in the LSRII or Cytoflex. Further analysis and generation of plots was completed using the Kaluza software v1.5a (BD).

Slice dissociation and single-cell RNA library preparation

Single-cell dissociation of mPSs. For dissociation, slices were washed 3X with room temperature (RT) dPBS and then transferred into 15 ml (2 slices/5 mL) of prewarmed (37 °C) TrypLE Express dissociation buffer (Gibco-Thermo Fisher. Waltham, MA), vortexed briefly, and incubated in a 37 °C water bath for 10 min, shaking occasionally. The vortex was set to medium speed and the preparation vortexed 10X with 4–5 s blasts before returning to the water bath for an additional 2 min. The vortex step was repeated, and the cells incubated for one more minute. Immediately afterwards, 20 mL of wash buffer (PBS plus 100 mg/ml of Trypsin Inhibitor from Glycine, 10 mg/ml Aprotinin, 10 mg/ml Chymostatin and 10% fetal bovine serum) were added, and the preparation shaken well and centrifuged at 1500 RPM for 5 min. The supernatant was discarded, and the pellet resuspended in 20 mL of wash buffer. The suspension was then passed through 100 mm filter. The centrifugation and resuspension steps were repeated and the pellet passed through a 40 mm filter to obtain a single cell suspension. Most of the residual agarose should be removed at this stage. The suspension was centrifuged again, and the pellet resuspended in 200 µl of cold PBS. A 10 µl aliquot was taken for counting and viability assessment with Trypan blue. Viability should be no less than 80%. The optimal recommended concentration was 1000 cells/µl (minimum: 300 cells/µl). The tube was kept on ice and submitted immediately for sequencing to the Center for Genome Technology (CGT), John P. Hussman Institute for Human Genomics at the University of Miami Miller School of Medicine.

Single-cell RNA library preparation and sequencing. Single-cell RNA libraries were generated using the Chromium Single Cell 3′ kit (10X Genomics, CA, USA). Cells were counted with a hemocytometer and diluted to target ~10,000 single-cell gel beads in emulsions (GEMs) per sample, except for the THR sample, where 20,000 cells were

targeted. Samples were processed according to the manufacturer's specifications using the Chromium Controller. Sequencing libraries were evaluated for quality using the Agilent TapeStation and quantified with a Qubit 2.0 Fluorometer. Pooled libraries were further quantified using qPCR before being loaded onto an Illumina NovaSeq 6000 S2 flow cell. Sequencing was performed in line with 10X Genomics' guidelines. Raw sequence data (.bcl files) were converted to fastq files and demultiplexed using CellRanger mkfastq. Subsequent UMI and cell barcode deconvolution, as well as genome mapping, were performed using the CellRanger software pipeline (version 3.0.0), resulting in digital gene expression matrices and Cloupe files. This methodology ensured the isolation of viable single cells from pancreatic slice cultures, suitable for high-quality scRNA-seq analysis. The approach effectively balanced cell viability and yield across the three experimental groups, facilitating subsequent genomic analyses.

Bioinformatics processing of single-cell RNA sequencing data

Quality control and Data Correction. Quality control and data correction were performed for each single-cell sample based on the number of detected genes and the percentage of mitochondrial genes. Specifically, samples with fewer than 200 genes, more than 8000 genes, fewer than 200 molecules, or more than 20% mitochondrial genes were excluded. The remaining data from three datasets were combined, and the same process was followed for three additional combined datasets. Single-cell libraries were sequenced, aligned to the human reference genome, filtered for quality control, and subjected to unsupervised clustering, integration, and differential gene expression analysis using the Seurat package. Cell identities were validated by examining cell type-specific marker genes and transcriptional signatures.

Integration and dimensionality reduction. Following quality control, the Seurat R package (v4.1.1) was used to process the data. Reciprocal PCA (RPCA) was employed for the integration of scRNA-seq datasets. The RPCA integration method projects each dataset into the other's PCA space and confines the anchors by the same mutual neighborhood constraint. Post-integration, the NormalizeData() function was used to "LogNormalize" the count data. A shared nearest neighbor (SNN) modularity optimization-based clustering algorithm and the Uniform Manifold Approximation and Projection (UMAP) algorithm were utilized to project all cells into two-dimensional coordinates for visualization.

Assignment of identity to clusters and pathway analysis. To identify the cell types within clusters (UMAP), we utilized the FindAllMarkers() function in the Seurat package with default settings (min.pct = 0.25, logfc.threshold = 0.25). The most significantly expressed genes in each cluster were used for cell type identification. The PanglaoDB database and the Enrichr tool were used to assign cell identities accurately. Gene Ontology (GO) analyses were performed using Enrichr.

Sub-clustering of UMAP clusters. We subsetted the Endoc and H2 clusters from the UMAP of Alloxan+THR, excluding all other clusters, and performed re-clustering using Seurat to obtain four new clusters: H2.1, H2.2, H2.3, and Endoc. Further sub-setting and re-clustering of the Endoc cluster resulted in three additional clusters: 1, 2, and 3. Two sub-groups within cluster 1 were identified manually by creating a ggplot2-based scatter plot (e.g., using DimPlot() or FeaturePlot()) and selecting cells interactively with CellSelector(), assigning them as beta cells A and B.

RNA Velocity Analysis. RNA velocity analysis was performed using the scVelo package. Initially, the gene expression matrix was preprocessed by filtering genes and cells based on minimum expression thresholds and normalizing the data with the scv.pp.filter_and_normalize function. Moments necessary for RNA velocity estimation were then computed using principal components and nearest neighbors through scv.pp.moments. Subsequent steps for RNA velocity computation included:

1. Velocity Computation: RNA velocities were estimated using the dynamical model implemented in scVelo (scv.tl.velocity).
2. Velocity Graph Construction: A velocity graph, representing potential future states of cells based on RNA velocity, was constructed (scv.tl.velocity_graph).

Latent time, which represents the cell's position along the inferred developmental trajectory, was computed using scv.tl.latent_time. This step incorporates RNA velocities to provide a temporal ordering of cells. For dimensionality reduction and visualization of the high-dimensional single-cell RNA-seq data, UMAP was employed. The UMAP coordinates were computed using the scanpy package (sc.tl.umap). To infer connectivity between cell clusters and visualize the overall structure of cell state transitions, the PAGA algorithm implemented in scVelo was used. PAGA computation was based on pre-identified cell clusters (Seurat clusters) using scv.tl.paga. The PAGA transition confidence matrix was then adjusted to reflect transitions based on latent time, ensuring that transitions followed the direction of increasing latent time and thereby maintaining biological relevance to the inferred cell trajectories.

Transition score analysis. We calculated normalized scores for each cell based on the frequency of gene expression associated with endocrine, ductal, and acinar cell types. The overall normalized score for each cell was computed using the formula:

$$\begin{aligned} \textit{Normalized Score} = (10 \times \textit{Endocrine Gene Count}) - \\ (5 \times \textit{Ductal Gene Count}) - (5 \times \textit{Acinar Gene Count}) \end{aligned}$$

This approach ensured that cells predominantly expressing endocrine-associated genes received higher scores, while the presence of ductal and acinar gene expression reduced the overall score. The normalized scores were then used to assign colors to each cell for visualization in UMAP plots. Specifically, cells with scores ranging from 85 to 100 were colored red, representing high endocrine gene expression with minimal or no ductal and acinar gene contributions. Scores between 50 and 84 were assigned a gradient color in the purple palette, while scores between 0 and 49 were assigned a blue gradient color. Cells with undefined or missing scores were colored grey. These color assignments were mapped onto the UMAP plots to visualize the spatial distribution of cells according to their normalized scores.

Pie Chart analysis. For the pie chart analysis, we began by selecting the 15 most prominent genes associated with ductal, acinar, and endocrine cell types, respectively. We then sorted all genes within each cell based on their RNA counts, from highest to lowest, focusing on these 45 genes. Next, we examined the top 10 highest expressing genes in each cell and counted how many of these belonged to the endocrine, ductal, or acinar categories. Cells where 9 or 10 of the top 10 genes were endocrine-associated were assigned a red color, indicating a predominantly endocrine identity. Conversely, cells with fewer than 8 endocrine genes, combined with an increase in ductal or acinar genes (more than 1), were considered ductoacinar cells and were assigned a blue color.

Statistical analysis

Statistical differences between groups were determined using unpaired two-tailed t-test, with 95% confidence intervals ($*p < 0.05$; $**p < 0.01$; $***p < 0.001$) after the Shapiro-Wilk normality test. Kruskal Wallis or Ordinary One-way Anova was conducted for three groups, when appropriate. The findings are shown as mean ± standard error (SE). GraphPad Prism v8 was used to analyze the data and create the graphics.

Reporting summary

Further information on research design is available in the Nature Portfolio Reporting Summary linked to this article.

Data availability

All raw and processed single-cell RNA-seq data generated in this study have been deposited in the NCBI Gene Expression Omnibus under accession number GSE274591. Count matrices, metadata, and CellRanger outputs are included as part of that record. Data underlying graphs and quantitative analysis are provided in the Source Data File. Source data are provided with this paper.

Code availability

All analysis scripts—including Seurat v4.1.1 workflows for clustering, UMAP/SpatialDimPlot visualizations, differential expression, scVelo PAGA, and imaging analyses—are publicly available in the GitHub repository JDBLab/Pancreatic-beta-cell-regeneration-by-THR-123: V1.2.0. This exact snapshot has been archived on Zenodo with https://doi.org/10.5281/zenodo.15684171.

References

1. Qadir, M. M. F. et al. P2RY1/ALK3-expressing cells within the adult human exocrine pancreas are BMP-7 expandable and exhibit progenitor-like characteristics. *Cell Rep.* **22**, 2408–2420 (2018).
2. Dirice, E. et al. Single-nucleus RNA-Seq reveals singular gene signatures of human ductal cells during adaptation to insulin resistance. *JCI Insight* **7**, e153877 (2022).
3. Qadir, M. M. F. et al. Single-cell resolution analysis of the human pancreatic ductal progenitor cell niche. *Proc. Natl. Acad. Sci. USA* **117**, 10876–10887 (2020).
4. Hendley, A. M. et al. Single-cell transcriptome analysis defines heterogeneity of the murine pancreatic ductal tree. *eLife* **10**, e67776 (2021).
5. Qadir, M. M. F. et al. Long-term culture of human pancreatic slices as a model to study real-time islet regeneration. *Nat. Commun.* **11**, 3265 (2020).
6. Doke, M. et al. Dynamic scRNA-seq of live human pancreatic slices reveals functional endocrine cell neogenesis through an intermediate ducto-acinar stage. *Cell Metab.* **35**, 1944–1960 e1947 (2023).
7. Sugimoto, H. et al. Activin-like kinase 3 is important for kidney regeneration and reversal of fibrosis. *Nat. Med.***18**, 396–404 (2012).
8. Salido-Medina, A. B. et al. BMP7-based peptide agonists of BMPR1A protect the left ventricle against pathological remodeling induced by pressure overload. *Biomed. Pharmacother.* **149**, 112910 (2022).
9. Carlson, W. D., Keck, P. C., Bosukonda, D. & Carlson, F. R. Jr A process for the design and development of novel bone morphogenetic protein-7 (BMP-7) mimetics with an example: THR-184. *Front. Pharm.* **13**, 864509 (2022).
10. Himmelfarb, J. et al. Perioperative THR-184 and AKI after cardiac surgery. *J. Am. Soc. Nephrol.* **29**, 670–679 (2018).
11. Benoit, S. W. & Devarajan, P. Acute kidney injury: emerging pharmacotherapies in current clinical trials. *Pediatr. Nephrol.* **33**, 779–787 (2018).
12. Bosukonda, A. & Carlson, W. D. Harnessing the BMP signaling pathway to control the formation of cancer stem cells by effects on epithelial-to-mesenchymal transition. *Biochem. Soc. Trans.* **45**, 223–228 (2017).
13. Dor, Y., Brown, J., Martinez, O. I. & Melton, D. A. Adult pancreatic beta-cells are formed by self-duplication rather than stem-cell differentiation. *Nature* **429**, 41–46 (2004).
14. Klein, D. et al. BMP-7 induces adult human pancreatic exocrine-to-endocrine conversion. *Diabetes* **64**, 4123–4134 (2015).
15. Rezanejad, H. et al. Heterogeneity of SOX9 and HNF1beta in pancreatic ducts is dynamic. *Stem Cell Rep.* **10**, 725–738 (2018).
16. Dominguez-Bendala, J., Qadir, M. M. F. & Pastori, R. L. Pancreatic progenitors: there and back again. *Trends Endocrinol. Metab.* https://doi.org/10.1016/j.tem.2018.10.002 (2018).
17. Chattopadhyay, T., Singh, R. R., Gupta, S. & Surolia, A. Bone morphogenetic protein-7 (BMP-7) augments insulin sensitivity in mice with type II diabetes mellitus by potentiating PI3K/AKT pathway. *Biofactors* **43**, 195–209 (2017).
18. Maric, I. et al. BMP signaling in rats with TNBS-induced colitis following BMP7 therapy. *Am. J. Physiol. Gastrointest. Liver Physiol.* **302**, G1151–G1162 (2012).
19. Rocher, C. & Singla, D. K. SMAD-PI3K-Akt-mTOR pathway mediates BMP-7 polarization of monocytes into M2 macrophages. *PLoS One* **8**, e84009 (2013).
20. Kuo, M. M. et al. BMP-9 as a potent brown adipogenic inducer with anti-obesity capacity. *Biomaterials* **35**, 3172–3179 (2014).
21. Blaine, S. A. et al. Adult pancreatic acinar cells give rise to ducts but not endocrine cells in response to growth factor signaling. *Development* **137**, 2289–2296 (2010).
22. El-Gohary, Y. et al. Intra-islet pancreatic ducts can give rise to insulin-positive cells. *Endocrinology* en20151175, https://doi.org/10.1210/en.2015-1175 (2015).
23. Bouwens, L., Braet, F. & Heimberg, H. Identification of rat pancreatic duct cells by their expression of cytokeratins 7, 19, and 20 in vivo and after isolation and culture. *J. Histochem Cytochem* **43**, 245–253 (1995).
24. Dahiya, S. et al. Acinar to beta-like cell conversion through inhibition of focal adhesion kinase. *Nat. Commun.* **15**, 3740 (2024).
25. Pasquali, L., Fan, Y., Trucco, M. & Ringquist, S. Rehabilitation of adaptive immunity and regeneration of beta cells. *Trends Biotechnol.* **24**, 516–522 (2006).
26. Alver, C. G. et al. SliceChip: a benchtop fluidic platform for organotypic culture and serial assessment of human and rodent pancreatic slices. *Lab Chip*, https://doi.org/10.1039/d3lc00850a (2024).
27. Marciniak, A. et al. Using pancreas tissue slices for in situ studies of islet of Langerhans and acinar cell biology. *Nat. Protoc.* **9**, 2809–2822 (2014).
28. Mao, X. et al. Single-cell transcriptomic analysis of the mouse pancreas: characteristic features of pancreatic ductal cells in chronic pancreatitis. *Genes.***13**, 1015 (2022).
29. Iwama, H. et al. Cathepsin B and D deficiency in the mouse pancreas induces impaired autophagy and chronic pancreatitis. *Sci. Rep.* **11**, 6596 (2021).
30. Al-Hasani, K. et al. Inhibition of pancreatic EZH2 restores progenitor insulin in T1D donor. *Signal Transduct. Target Ther.* **7**, 248 (2022).
31. Giarrizzo, M., LaComb, J. F. & Bialkowska, A. B. The role of kruppel-like factors in pancreatic physiology and pathophysiology. *Int. J. Mol. Sci.* **24**, https://doi.org/10.3390/ijms24108589 (2023).
32. Baldan, J. et al. Resolution of acinar dedifferentiation regulates tissue remodeling in pancreatic injury and cancer initiation. *Gastroenterology*, https://doi.org/10.1053/j.gastro.2024.04.031 (2024).
33. Naganuma, S. et al. Nuclear translocation of H2RSP is impaired in regenerating intestinal epithelial cells of murine colitis model. *Virchows Arch.* **448**, 354–360 (2006).
34. Vimalachandran, D. et al. High nuclear S100A6 (Calcyclin) is significantly associated with poor survival in pancreatic cancer patients. *Cancer Res.* **65**, 3218–3225 (2005).
35. Rubin, C. I. & Atweh, G. F. The role of stathmin in the regulation of the cell cycle. *J. Cell Biochem* **93**, 242–250 (2004).
36. Zhu, P. et al. C8orf4 negatively regulates self-renewal of liver cancer stem cells via suppression of NOTCH2 signalling. *Nat. Commun.* **6**, 7122 (2015).
37. Zhang, P. et al. The high expression of TC1 (C8orf4) was correlated with the expression of beta-catenin and cyclin D1 and the

progression of squamous cell carcinomas of the tongue. *Tumour Biol.* **36**, 7061–7067 (2015).
38. Wells, J. M. et al. Wnt/beta-catenin signaling is required for development of the exocrine pancreas. *BMC Dev. Biol.* **7**, 4 (2007).
39. Nusse, R. Wnt signaling and stem cell control. *Cell Res.* **18**, 523–527 (2008).
40. Whim, M. D. Pancreatic beta cells synthesize neuropeptide Y and can rapidly release peptide co-transmitters. *PLoS ONE* **6**, e19478 (2011).
41. Rodnoi, P. et al. Neuropeptide Y expression marks partially differentiated beta cells in mice and humans. *JCI Insight* **2**, e94005 (2017).
42. El-Gohary, Y. et al. A Smad signaling network regulates islet cell proliferation. *Diabetes* **63**, 224–236 (2014).
43. Kim, S. et al. Molecular and genetic regulation of pig pancreatic islet cell development. *Development* **147**, dev186213 (2020).
44. Lemaire, K., Thorrez, L. & Schuit, F. Disallowed and allowed gene expression: two faces of mature islet beta cells. *Annu. Rev. Nutr.* **36**, 45–71 (2016).
45. Li, H., Neelankal John, A., Nagatake, T., Hamazaki, Y. & Jiang, F. X. Claudin 4 in pancreatic beta cells is involved in regulating the functional state of adult islets. *FEBS Open Bio* **10**, 28–40 (2020).
46. Min, B. H. et al. Clusterin expression in the early process of pancreas regeneration in the pancreatectomized rat. *J. Histochem Cytochem* **51**, 1355–1365 (2003).
47. Kim, B. M. et al. Clusterin induces differentiation of pancreatic duct cells into insulin-secreting cells. *Diabetologia* **49**, 311–320 (2006).
48. Lee, S. et al. Essential role of clusterin in pancreas regeneration. *Dev. Dyn.* **240**, 605–615 (2011).
49. Zhao, R. et al. Single-cell heterogeneity analysis and CRISPR screens in MIN6 cell line reveal transcriptional regulators of insulin. *Cell Cycle* **20**, 2053–2065 (2021).
50. Fernandez, A. et al. A single-cell atlas of the murine pancreatic ductal tree identifies novel cell populations with potential implications in pancreas regeneration and exocrine pathogenesis. *Gastroenterology*, https://doi.org/10.1053/j.gastro.2024.06.008 (2024).
51. Bergen, V., Lange, M., Peidli, S., Wolf, F. A. & Theis, F. J. Generalizing RNA velocity to transient cell states through dynamical modeling. *Nat. Biotechnol.* **38**, 1408–1414 (2020).
52. La Manno, G. et al. RNA velocity of single cells. *Nature* **560**, 494–498 (2018).
53. Dominguez-Bendala, J., Qadir, M. M. F. & Pastori, R. L. Temporal single-cell regeneration studies: the greatest thing since sliced pancreas?. *Trends Endocrinol. Metab.* **32**, 433–443 (2021).
54. Wolf, F. A. et al. PAGA: graph abstraction reconciles clustering with trajectory inference through a topology preserving map of single cells. *Genome Biol.* **20**, 59 (2019).
55. Panzer, J. K. et al. Pancreas tissue slices from organ donors enable in situ analysis of type 1 diabetes pathogenesis. *JCI Insight* **5**, e134525 (2020).
56. Bensley, R. R. Studies on the pancreas of the guinea pig. *Am. J. Anat.* **12**, 297–388 (1911).
57. Bonner-Weir, S. et al. Islet neogenesis: a possible pathway for beta-cell replenishment. *Rev. Diabet. Stud.* **9**, 407–416 (2012).
58. Magenheim, J. et al. Matters arising: Insufficient evidence that pancreatic beta cells are derived from adult ductal Neurog3-expressing progenitors. *Cell Stem Cell* **30**, 488–497.e483 (2023).
59. Mandyam, C. D., Harburg, G. C. & Eisch, A. J. Determination of key aspects of precursor cell proliferation, cell cycle length and kinetics in the adult mouse subgranular zone. *Neuroscience* **146**, 108–122 (2007).
60. Waghmare, S. K. et al. Quantitative proliferation dynamics and random chromosome segregation of hair follicle stem cells. *EMBO J.* **27**, 1309–1320 (2008).
61. Mead, T. J. & Lefebvre, V. Proliferation assays (BrdU and EdU) on skeletal tissue sections. *Methods Mol. Biol.* **1130**, 233–243 (2014).
62. Bruun, C. et al. Inhibition of beta cell growth and function by bone morphogenetic proteins. *Diabetologia* **57**, 2546–2554 (2014).
63. Sugimoto, H. et al. BMP-7 functions as a novel hormone to facilitate liver regeneration. *FASEB J.* **21**, 256–264 (2007).
64. Kim, M. & Choe, S. BMPs and their clinical potentials. *BMB Rep.* **44**, 619–634 (2011).
65. White, A. P. et al. Clinical applications of BMP-7/OP-1 in fractures, nonunions and spinal fusion. *Int Orthop.* **31**, 735–741 (2007).
66. Ward, J. M., Uno, H., Kurata, Y., Weghorst, C. M. & Jang, J. J. Cell proliferation not associated with carcinogenesis in rodents and humans. *Environ. Health Perspect.* **101**, 125–135 (1993).
67. Valdez, I. A. et al. Proinflammatory cytokines induce endocrine differentiation in pancreatic ductal cells via STAT3-dependent NGN3 activation. *Cell Rep.* **15**, 460–470 (2016).
68. Wang, P. et al. A high-throughput chemical screen reveals that harmine-mediated inhibition of DYRK1A increases human pancreatic beta cell replication. *Nat. Med.* **21**, 383–388 (2015).
69. Wang, P. et al. Select DYRK1A inhibitors enhance both proliferation and differentiation in human pancreatic beta cells. *bioRxiv*, https://doi.org/10.1101/2024.05.17.594179 (2024).
70. Al-Hasani, K. et al. EZH2 inhibitors promote beta-like cell regeneration in young and adult type 1 diabetes donors. *Signal Transduct. Target. Ther.* **9**, 2 (2024).
71. Dominguez-Bendala, J. & Ricordi, C. Present and future cell therapies for pancreatic beta cell replenishment. *World J. Gastroenterol.* **18**, 6876–6884 (2012).
72. Rickels, M. R. et al. Long-term outcomes with islet-alone and islet-after-kidney transplantation for type 1 diabetes in the clinical islet transplantation consortium: the CIT-08 study. *Diab Care* **45**, 2967–2975 (2022).
73. Hogrebe, N. J., Ishahak, M. & Millman, J. R. Developments in stem cell-derived islet replacement therapy for treating type 1 diabetes. *Cell Stem Cell* **30**, 530–548 (2023).
74. Lynch, K. L., Gooding, L. R., Garnett-Benson, C., Ornelles, D. A. & Avgousti, D. C. Epigenetics and the dynamics of chromatin during adenovirus infections. *FEBS Lett.* **593**, 3551–3570 (2019).
75. Chu, C. M. J. et al. Dynamic Ins2 gene activity defines beta-cell maturity states. *Diabetes* **71**, 2612–2631 (2022).
76. Dominguez-Bendala, J. & Bonner-Weir, S. Bend it like Occam: ductal origin of new islet cells in human pancreas after injury. *Diabetes* **74**, 1–3 (2025).
77. Kilic, G. et al. The islet estrogen receptor-alpha is induced by hyperglycemia and protects against oxidative stress-induced insulin-deficient diabetes. *PLoS ONE* **9**, e87941 (2014).
78. Deeds, M. C. et al. Single dose streptozotocin-induced diabetes: considerations for study design in islet transplantation models. *Lab Anim.* **45**, 131–140 (2011).
79. Maxwell, K. G., Kim, M. H., Gale, S. E. & Millman, J. R. Differential function and maturation of human stem cell-derived islets after transplantation. *Stem Cells Transl. Med.* **11**, 322–331 (2022).
80. Mather, K. Surrogate measures of insulin resistance: of rats, mice, and men. *Am. J. Physiol. Endocrinol. Metab.* **296**, E398–E399 (2009).
81. Marciniak, A., Selck, C., Friedrich, B. & Speier, S. Mouse pancreas tissue slice culture facilitates long-term studies of exocrine and endocrine cell physiology in situ. *PLoS ONE* **8**, e78706 (2013).

Acknowledgements

In memoriam: Gary Kleiman (1953–2024). We wish to thank Paul Latta as well as Felipe Echeverri and Ramón Poo (Biorep), Maria Boulina (DRI-Imaging Core), Oliver Umland (DRI-Flow Cytometry Core) Kevin Johnson (DRI-Histology Core) and Amira Mansouri, Sarah Mohammed, Emilio Canales, and Yaisa Moreno, while training at our laboratory. This work

was funded by the Diabetes Research Institute Foundation (DRIF), Lainoff Family Foundation, Gary Kleiman Memorial Fund, Tonkinson Foundation, Inserra Family Foundation, the Foundation for Diabetes Research, Vega Clara Fund, and the Peacock Foundation; NIH grants 1R01DK138210-01, 1R01DK130846-01 and U01DK120393; ADA award 1-19-ICTS-078, and JDRF award 3-SRA-2024-1518-S-B. Human samples were provided by the Network for Pancreatic Organ Donors with Diabetes (nPOD;RRID:SCR_014641), a collaborative type 1 diabetes research project sponsored by JDRF (nPOD:5-SRA-2018-557-Q-R) and The Leona M. & Harry B. Helmsley Charitable Trust (Grant#2018PG-T1D053), as well as The Helmsley Charitable Trust George S. Eisenbarth nPOD Award for Team Science (2015-PG-T1D-052). Finally, we wholeheartedly thank the donors and their families for their invaluable contribution to science. Drs. Domínguez-Bendala and Ricardo Pastori are the guarantors of this work and, as such, had full access to all the data and take responsibility for the integrity and the accuracy of the analysis.

Author contributions

S.A.-C, I.A., M.D., and D.K.: Discussion/advice on experimental design, data collection/analysis/interpretation, and manuscript writing and review. A.T., O.A., C.G.S., C.G.A., F.C., O.B., D.T., and B.N.-R.: Data collection/analysis/interpretation. M.M.F.Q., C.R., A.C., P.B., and A.A.: Discussion/advice on experimental design, research support, and critical reading of the manuscript. E.O.: Co-mentored S.A.-C's thesis. R.L.P. and J.D.-B.: Conception/design of the study, data analysis/interpretation and manuscript writing.

Competing interests

Drs. Domínguez-Bendala, Pastori and Ricordi are named inventors in the patent titled: Compositions, Systems and Methods for Obtaining Insulin-Producing Cells, U.S. Patent No. 11,466,255 B2 (October 11, 2022). Drs. Domínguez-Bendala and Ricordi are also named inventors in the patents titled: Enhanced Oxygen Cell Culture Platforms; Patent number: 8,551,770 (July 11, 2013); and Enhanced Oxygen Cell Culture Platforms (CIP), Patent number: 9,175,254 (September 17, 2015). The University of Miami and Dr. Juan Domínguez-Bendala et al. hold the rights to intellectual property used in the study and may financially benefit from the commercialization of the intellectual property. All other authors declare no competing interests.

Additional information

Supplementary information The online version contains supplementary material available at https://doi.org/10.1038/s41467-025-61534-2.

Correspondence and requests for materials should be addressed to Ricardo Luis Pastori or Juan Domínguez-Bendala.

Peer review information *Nature Communications* thanks the anonymous reviewers for their contribution to the peer review of this work. A peer review file is available.

Reprints and permissions information is available at http://www.nature.com/reprints

Publisher's note Springer Nature remains neutral with regard to jurisdictional claims in published maps and institutional affiliations.

Open Access This article is licensed under a Creative Commons Attribution-NonCommercial-NoDerivatives 4.0 International License, which permits any non-commercial use, sharing, distribution and reproduction in any medium or format, as long as you give appropriate credit to the original author(s) and the source, provide a link to the Creative Commons licence, and indicate if you modified the licensed material. You do not have permission under this licence to share adapted material derived from this article or parts of it. The images or other third party material in this article are included in the article's Creative Commons licence, unless indicated otherwise in a credit line to the material. If material is not included in the article's Creative Commons licence and your intended use is not permitted by statutory regulation or exceeds the permitted use, you will need to obtain permission directly from the copyright holder. To view a copy of this licence, visit http://creativecommons.org/licenses/by-nc-nd/4.0/.

© The Author(s) 2025